

**University of Alberta**

**Influence of Head Volume Conductor Accuracy and *a priori* Constraints on Inverse  
Source Localization for Epileptic Patients in a Clinical Context**

by

Natasha L. Kuzbik



A thesis submitted to the Faculty of Graduate Studies and Research  
in partial fulfillment of the requirements for the degree of

**Master of Science**

Department of Electrical and Computer Engineering  
Department of Biomedical Engineering

Edmonton, Alberta

Fall 2007



Library and  
Archives Canada

Bibliothèque et  
Archives Canada

Published Heritage  
Branch

Direction du  
Patrimoine de l'édition

395 Wellington Street  
Ottawa ON K1A 0N4  
Canada

395, rue Wellington  
Ottawa ON K1A 0N4  
Canada

*Your file* *Votre référence*  
*ISBN: 978-0-494-33289-4*  
*Our file* *Notre référence*  
*ISBN: 978-0-494-33289-4*

**NOTICE:**

The author has granted a non-exclusive license allowing Library and Archives Canada to reproduce, publish, archive, preserve, conserve, communicate to the public by telecommunication or on the Internet, loan, distribute and sell theses worldwide, for commercial or non-commercial purposes, in microform, paper, electronic and/or any other formats.

The author retains copyright ownership and moral rights in this thesis. Neither the thesis nor substantial extracts from it may be printed or otherwise reproduced without the author's permission.

**AVIS:**

L'auteur a accordé une licence non exclusive permettant à la Bibliothèque et Archives Canada de reproduire, publier, archiver, sauvegarder, conserver, transmettre au public par télécommunication ou par l'Internet, prêter, distribuer et vendre des thèses partout dans le monde, à des fins commerciales ou autres, sur support microforme, papier, électronique et/ou autres formats.

L'auteur conserve la propriété du droit d'auteur et des droits moraux qui protègent cette thèse. Ni la thèse ni des extraits substantiels de celle-ci ne doivent être imprimés ou autrement reproduits sans son autorisation.

---

In compliance with the Canadian Privacy Act some supporting forms may have been removed from this thesis.

Conformément à la loi canadienne sur la protection de la vie privée, quelques formulaires secondaires ont été enlevés de cette thèse.

While these forms may be included in the document page count, their removal does not represent any loss of content from the thesis.

Bien que ces formulaires aient inclus dans la pagination, il n'y aura aucun contenu manquant.

  
**Canada**

# Abstract

The location of the neural source causing epileptic seizures can be found by solving the inverse problem from the EEG signal. This study analyzed the effects of head model precision and *a priori* information on accuracy of inverse source localization results.

Inaccurate representation of geometric and electromagnetic properties of the head and electrode positioning on the scalp may propagate as errors in the inverse problem. We found that variations in conductivity properties and electrode positioning affected source localization, while segmentation errors did not have a significant effect.

Two *a priori* constraints were incorporated into the inverse problem. The source orientation was restricted normal to the cortical surface and information from Single Photon Emission Computed Tomography (SPECT) functional images was incorporated. Both constraints had a significant impact on source localization accuracy.

# Acknowledgements

Thanks to my supervisor Dr. Z. Koles for both financial and technical support, providing me with valuable expertise needed for my thesis study. My appreciation is also extended to all of my colleagues within the Medical Image and Signal Processing research lab for their technical and moral support. Thank you also to my colleagues from the Department of Biomedical Engineering and the Department of Electrical and Computer Engineering for continued discussions and advice. Completion of MRI segmentation would not have been possible without the help of Dan Withey and Doug Vujanic.

I would like to express sincere gratitude to all of my friends and family for their constant encouragement – thank you for being there for me through thick and thin! I especially appreciate Aisha Yahya’s constant reviews, advice, and praise – and thank you for making me laugh no matter what! Thanks to Mom, Dad, and Jana for being such a constant force in my life, the support that I can always count on. Finally, I am forever grateful for meeting Chris Raffa, who accepts all of me for who I am while at the same time encouraging me to learn and grow.

# Table of Contents

<b>1</b>	<b>Introduction</b>	<b>1</b>
<b>2</b>	<b>Background and Fundamentals</b>	<b>4</b>
2.1	Epilepsy	4
2.2	Electroencephalogram	5
2.2.1	EEG Instrumentation	5
2.2.2	EEG Signal	8
2.3	Inverse Problem	10
2.3.1	Source Model for the Inverse Problem	11
2.3.2	Head Model for the Inverse Problem	11
2.3.2.1	Lead Field Matrix	13
2.3.3	Source Localization Methods	14
2.3.3.1	Dipolar Models	15
2.3.3.2	Distributed Source Models	16
<b>3</b>	<b>Accuracy of Inverse Source Localization</b>	<b>19</b>
3.1	Lead Field Matrix Accuracy	19
3.2	<i>a priori</i> Information	23
3.2.1	Normal Dipolar Source Orientation	23
3.2.2	Functional Imaging Information	23
<b>4</b>	<b>Setup of Head Model and Inverse Problem</b>	<b>27</b>
4.1	Realistic Head Model from MRI	27
4.1.1	Setup of Solution Space	31
4.1.2	Electrode Locations on the Head Model	33
4.1.3	Calculation of the Lead Field Matrix	35
4.2	Inverse Problem	38
4.2.1	Normal Dipolar Orientation Constraint	41
4.2.2	Incorporation of SPECT Image Information	42
<b>5</b>	<b>Computer Simulations and Results</b>	<b>43</b>
5.1	Validation Metrics	46
5.2	Head Model Setup for Lead Field Matrix Analysis	48
5.2.1	Electrode Positioning	48
5.2.2	Electrode Distribution	49
5.2.3	CSF-Skull Boundary Delineation	49
5.2.4	Variations in Skull-to-Brain Conductivity Ratio	49
5.2.5	White Matter Anisotropy	50
5.3	Inverse Problem Setup for <i>a priori</i> Constraints	50
5.3.1	Normal Dipolar Orientation	50
5.3.2	SPECT Information	51

<b>5.4</b>	<b>Results</b>	<b>53</b>
5.4.1	Effects of Lead Field Matrix Accuracy	58
5.4.1.1	Electrode Positioning	58
5.4.1.2	Electrode Distribution	61
5.4.1.3	CSF-Skull Boundary Delineation	62
5.4.1.4	Skull-to-Brain Conductivity Ratio	62
5.4.1.5	White Matter Anisotropy	66
5.4.2	Effects of <i>a priori</i> Constraints	69
5.4.2.1	Normal Orientation Constraint	69
5.4.2.2	SPECT Information Constraint	70
<b>6</b>	<b>Discussion</b>	<b>81</b>
6.1	Head Model Precision	82
6.2	<i>a priori</i> Constraints	86
<b>7</b>	<b>Conclusions</b>	<b>92</b>
	<b>Future Considerations</b>	<b>94</b>
	<b>Bibliography</b>	<b>95</b>

# List of Tables

1	Resistivity values of segmented tissue.....	31
2	Displacement of electrodes.....	48
3	Mean values and (standard error of mean) for the Base Model.....	55
4	Mean and (standard error of mean) for the Base Model and for variations in the head model. ....	59

# List of Figures

1	Standard Electrode Placement Systems.....	7
2	Interconnected pyramidal cells are the main source of EEG signals.....	9
3	Example SPECT and SISCOM images from a patient.....	26
4	Segmentation results for a single MRI slice using mtrack tool.....	27
5	Segmentation of CSF tissue in MRI.....	29
6	Final MRI Segmentation Result.....	30
7	Smoothing the cortical surface.....	32
8	Electrodes positioned on the scalp surface of the head model.....	34
9	Finite Volume Method.....	36
10	Electrodes shift as center position of head model shifts.....	49
11	Qualitative setup for SPECT analysis.....	52
12	Source current density of time slice 185 for head model variations.....	56
13	Source current density of time slice 390 for head model variations.....	57
14	Validation metrics for variations in the skull-to-brain conductivity ratios.....	65
15	Source current density of time slice 185 for white matter orthotropic conductivity.....	67
16	Source current density of time slice 390 for white matter orthotropic conductivity.....	68
17	Source current density of time slice 185 for <i>a priori</i> constraints.....	71
18	Source current density of time slice 390 for <i>a priori</i> constraints.....	72
19	Center of mass error for different weighting levels of SPECT.....	73
20	Degree of Focalization for different weighting levels of SPECT.....	74



# Acronyms

**BEM** Boundary Element Method

**BET** Brain Extraction Tool

**BOLD** Blood Oxygenation Level Dependent

**CME** Center of Mass Error

**CSF** Cerebrospinal Fluid

**DF** Degree of Focalization

**DTI** Diffusion Tensor Magnetic Resonance Images

**EEG** Electroencephalogram

**FAST** FMRIB's Automated Segmentation Tool

**FEM** Finite Element Method

**fMRI** Functional Magnetic Resonance Images

**FOCUSS** Focal Underdetermined System Solution

**FSL** FMRIB Software Library

**FVM** Finite Volume Method

**LE** Localization Error

**LFM** Lead Field Matrix

**LORETA** Low Resolution Brain Electromagnetic Tomography

**MN** Minimum Norm Solution

**MRI** Magnetic Resonance Images

**SCD** Source Current Density

**SISCOM** Subtraction Ictal SPECT Coregistered to MRI

**SPECT** Single Photon Emission Computed Tomography

**SNR** Signal to Noise Ratio

**SVD** Singular Value Decomposition

**WMN** Weighted Minimum Norm Solution

# Chapter 1

## Introduction

Epilepsy is a neurological disorder that affects 1.3% of Canadians and presents itself in the form of seizures. An epileptic seizure is characterized by sudden and excessive electrical neural discharge in the grey matter of the brain. Approximately 60% of epileptic patients suffer from partial seizures (Siegel, 2004), which are seizures that originate in a localized region of the cortex (Shorvon, 2004). Patients with medically intractable partial seizures require surgery in order to remove the neural source causing seizures.

Pre-surgical investigation of epileptic patients attempts to identify the region of the brain that must be resected in order to eradicate seizures. This region of the cortex is termed the epileptogenic zone. Currently, pre-surgical clinical analysis is a multi-step process that involves the following: medical history and examination, psychiatric assessment, video-electroencephalogram (EEG) monitoring, magnetic resonance imaging (MRI), functional imaging, and neuropsychological evaluation (Shorvon, 2004; Siegel, 2004). Oftentimes the region of the cortex that needs to be resected cannot be resolved by these non-invasive inspections alone. Invasive inspection with intracranial EEG recordings is often required as well since it is difficult to localize accurately the epileptogenic zone with only non-invasive analysis (Siegel, 2004).

The electroencephalogram plays the most critical role in seizure detection because of its high temporal resolution and its ability to measure neural activity in real time both

during (ictal) and in between (interictal) epileptic seizures. Currently, clinical analysis of scalp EEG recordings involves qualitative inspection of the time series of the signal to locate electrode locations with deviations from normal waveforms. The location of the epileptogenic source is assumed to be the region of the brain associated with the electrodes with these abnormal waveforms. This visual analysis of the EEG recordings provides limited localization of the epileptogenic zone, often only indicating at best which lobe was involved during epileptic activity. Recently, research has focused on extracting more information from the EEG by mathematically solving the inverse problem for the neural source of the signal (Sherg and Von Cramon, 1986; Mosher et al., 1992; Scherg, 1992; Hämäläinen and Ilmoniemi, 1994; Gorodinsky et al., 1995; Pascual-Marqui, 1995; Koles and Soong, 1998; Fuschs et al., 2001; Liu et al., 2002; Grova et al., 2006). The solution of the inverse problem finds the underlying current distribution in the brain that best describes the potentials measured on the scalp. A realistic volume conductor model of the patient's head is required for the inverse problem to link the measured EEG signal to the bioelectric neural activity.

There is uncertainty in source localization because of the imprecision of the volume conductor model and the ill-posed nature of the inverse problem. The inverse problem is ill posed since an infinite number of distinct source configurations can generate the same potential distribution on the scalp and the solution is not stable with regard to small changes in data. Research has focused on improving source localization by introducing *a priori* information in order to reduce the number of possible solutions and to increase the stability of the problem (Dale and Sereno, 1993; Liu et al., 1998; Fuschs et al., 1999; Dale et al., 2000; Haueisen et al., 2002; Phillips et al., 2002a; Michel

et al., 2004; Lin et al., 2006). In addition, the volume conductor model has become progressively more realistic as a means to improve source localization accuracy (Dale and Sereno, 1993; Awada et al., 1998; Huiskamp et al., 1999; Cuffin et al., 2001; Baillet et al., 2001b; Liu et al., 2002; Ding et al., 2005; Grova et al., 2006; Lin et al., 2006; Liu et al., 2006; Ramon et al., 2006).

The purpose of this thesis is twofold: to study the effects of head model precision and *a priori* information on source localization accuracy. The ultimate goal of this research is to be able to incorporate EEG source localization techniques as a clinical pre-surgical tool for epileptic patients. To ensure feasibility in a clinical setting, the study is restricted to clinically available resources from the University of Alberta Hospital.

## Chapter 2

# Background and Fundamentals

### 2.1 Epilepsy

Epileptic seizures are classified as either partial or general. Partial seizures arise in a restricted region of the brain within one hemisphere, while general seizures involve both hemispheres of the brain from the onset (Shorvon, 2004). Partial seizures can be further classified as follows: simple partial, with the patient remaining conscious during the seizure; complex partial, with consciousness impaired during the episode; and partial secondary generalized, a partial seizure that evolves into a general seizure (Shorvon, 2004).

The most common form of treatment for epilepsy patients is long-term drug therapy. However, for some patients medication fails to control the epileptic seizures. For these cases, surgical resection of the cortical source of the seizures may be possible. Surgery is an option only if the seizure is confined to a small area (partial) that can be removed without having a significant negative impact on the person's brain function.

For some cases of epilepsy, a small region of the brain from which the seizure originates (epileptic focus) may be identified for surgical resection. However, some seizures involve a more widespread and complex network of neurons. Therefore, the term epileptogenic zone is used instead, which refers to the minimal amount of cortical area that needs to be surgically removed to ensure the eradication of seizures (Shorvon, 2004).

The irritative and ictal onset zones may also be identified during pre-surgical evaluation. The irritative zone is the area of the cortex that generates interictal spikes; this area may extend beyond the epileptogenic zone. The ictal onset zone is the region of the brain activated at the onset of the ictal EEG recording. This zone may give a rough indication of the target region for resection.

Currently, pre-surgical clinical analysis is a multi-step process that involves medical history and examination, psychiatric assessment, video-EEG monitoring, magnetic resonance imaging (MRI), functional imaging, and neuropsychological evaluation (Shorvon, 2004; Siegel, 2004). However, invasive inspection with intracranial EEG is often required since it is difficult to localize accurately the epileptogenic zone with non-invasive analysis (Siegel, 2004).

## **2.2 Electroencephalogram**

German psychiatrist Hans Berger developed the first human EEG instrument in the 1920s, measuring the electrical activity generated by nerve cells in the brain (Berger, 1929; Tyner, 1983). The EEG exhibits superior temporal resolution compared to other functional brain imaging techniques, but has poor spatial resolution. The relatively small number of electrodes measuring the scalp potential and the uncertainty of the inverse problem limit the spatial resolution of the EEG (Baillet et al., 2001a).

### **2.2.1 EEG Instrumentation**

EEG instrumentation consists of electrodes with conductive jelly, amplifiers, an A/D converter, and a recording device. The conductive jelly ensures minimum impedance between the skin and the electrode surface. The most common type of scalp electrodes are disks made of Ag-AgCl (Tyner, 1983). The potential difference between

electrodes placed on the scalp is amplified from microvolts to a level that can be digitized and recorded (Tyner, 1983). Two different electrode reference configurations are typically used: bipolar and unipolar. Bipolar electrodes measure the potential difference between pairs of electrodes, while unipolar electrodes measure the difference between each electrode and a reference electrode or each electrode and the average signal of all electrodes.

Figure 1 (A) and (B) display the standardized 10-20 electrode placement system (Jasper, 1958) used to place electrodes on the patient's scalp. The reference points of the coordinate system are the nasion (intersection of nasal and frontal bones on the skull), inion (most prominent projecting point of occipital bone at the base of the skull), and left and right preauricular points. The electrodes are placed at 10% and 20% intervals between these reference points, and labelled according to the region of the brain the electrode covers: C (central), F (frontal), O (occipital), P (parietal), and T (temporal). The labels on the left side of the head are odd numbers, while the right side are even.

Additional electrodes to the standard 21 electrodes of the 10-20 system montage can be added at intermediate 10% intervals, and labelled based on the standards of the American Electroencephalographic Society (Sharbrough et al., 1991). This new montage is termed the 10-10 system and is shown in Figure 1 (C). This system has been expanded yet again recently to the 10-5 system, with additional electrodes placed at intermediate 5% intervals (Oostenveld and Praamstra, 2001).



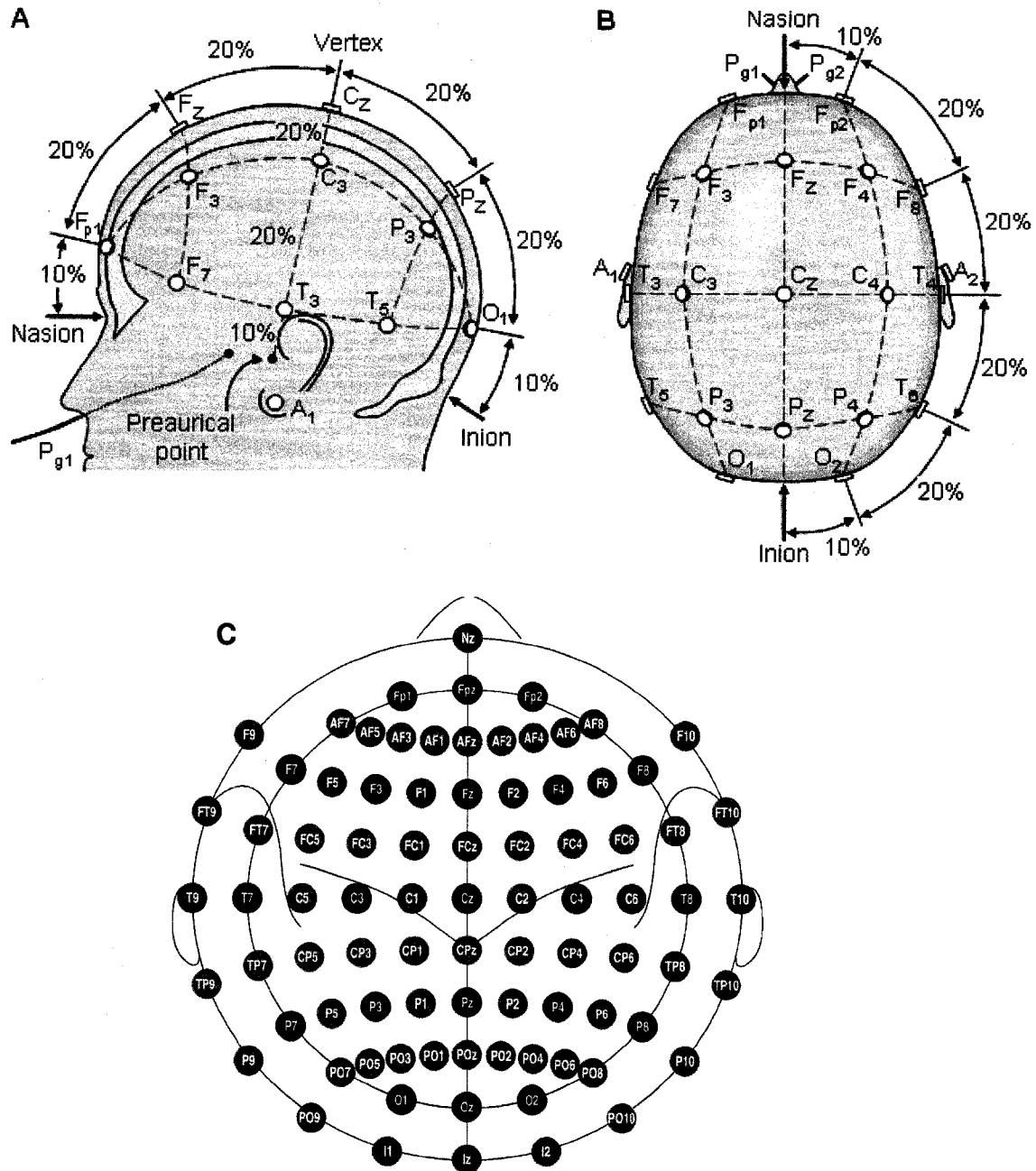


**Figure 1 Standard Electrode Placement Systems.** (A) and (B) show the 10-20 electrode placement system while (C) illustrates the 10-10 electrode placement system. The reference points for the system are the nasion, inion, and preauricular points. The electrodes are labelled according to the region of the brain covered: C (central), F (frontal), O (occipital), P (parietal), and T (temporal). The label Fp denotes the frontal polar region. The labels on the left side of the head are odd numbers, while the right side are even.

<sup>1</sup> Figure 1 (A) and (B) from: <http://butler.cc.tut.fi/~malmivuo/bem/bembook/13/13.htm>  
Figure 1 (C) from Oostenveld and Praamstra, 2001.

## 2.2.2 EEG Signal

Pyramidal cells situated in the cortical sheet generate all but the smallest magnitude of potentials measured by the scalp EEG. Figure 2 demonstrates the pyramidal cell activation within the cortical sheet. A single pyramidal cell excited by other neurons in the brain produces an excitatory postsynaptic potential (EPSP) at the apical dendrites of the cell (Hodgkin, 1964; Nunez, 1981). The membranes of the apical dendrites then depolarize, creating a negative extracellular charge with respect to the soma and distal basal dendrites of the same neuron. This depolarization causes primary current to flow intracellularly, and secondary current to flow extracellularly throughout the volume of the entire body to complete the flow loop (Hodgkin, 1964; Nunez, 1981; Baillet et al., 2001a).

The scalp electrodes cannot measure electrical potential from a single pyramidal cell because the magnitude of the potential is too small and the neuron location is too far from the scalp. Instead, the EEG measures the potential difference from a group of synchronously activated pyramidal cells. This is possible because the majority of pyramidal cells in the cortex are arranged together in columns perpendicular to the cortical surface. In addition, there are a large number of interconnections between the cortical neurons, with over  $10^3$  synapses per neuron, leading to synchronous activation of tens of thousands of pyramidal cells (Nunez, 1981). The potential difference from the cumulative sum of a group of simultaneously active pyramidal cells is large enough to measure on the scalp with electrodes.

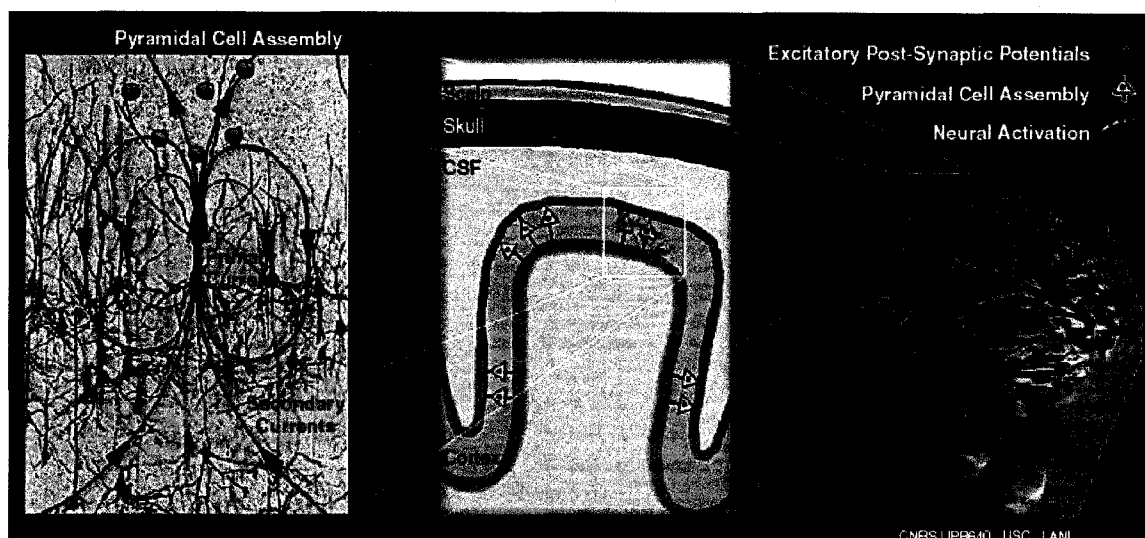


**Figure 2 Interconnected pyramidal cells are the main source of EEG signals.** (Left) An excited pyramidal cell produces an excitatory postsynaptic potential at the apical dendrites of the pyramidal cell, causing primary current to flow from the soma and basal dendrites to the apical dendrites. The current loop is closed by secondary currents that flow throughout the volume conductor. (Center, Left) The pyramidal cells are oriented in perpendicular columns that when activated simultaneously produce a potential difference large enough to measure on the scalp with electrodes. Baillet et al., 2001a

The potentials measured over time by the EEG have been categorized into four different sinusoidal groups of brain waves: beta, alpha, theta, and delta. Beta waves have the highest frequency ( $>13$  Hz) and are typically detected over the parietal and frontal lobes. The alpha waves have a frequency range of 8-13 Hz, measured from the occipital region of the brain when the patient's eyes are closed. The theta frequency is from 4-8 Hz, while the delta range is from 0.5-4Hz. The shape and frequency of EEG signals changes as the level of consciousness of a patient changes from awake to sleep.

One of the challenges with analyzing EEG signals is recognizing and eliminating artefacts. Physiological artefacts are from non-neural sources such as eye movements, cardiac and muscle activity, and changes in electrical activity of the skin. Non-physiological artefacts originate from such sources as electrode/switch contacts, cable movements, and 60Hz from the surrounding environment.

For epileptic patients, seizures are characterized by sudden and excessive neuronal discharges in the brain (Tyner, 1983). Due to this distinct electrophysiological activity, the EEG signal of an epileptic patient deviates from typical waveforms. Thus, scalp EEG recording can provide valuable information about the epileptogenic zone of the patient both during (ictal) and in between (interictal) seizures. A patient with epilepsy typically shows epileptiform abnormalities on the EEG recording during both of these periods. Interictal discharges consist of spikes or sharp waves, which are focal, multi-focal, or generalized (Duncan et al., 1995). Ictal EEG abnormalities usually show sustained, rhythmic activity with a variety of forms, depending on the type of seizure spread (Duncan et al., 1995).

### **2.3 Inverse Problem**

The inverse solution determines the source locations and magnitudes that best describe the potentials measured on the scalp. The relationship between the neuronal source configuration and the associated measured electrode potentials is mathematically represented by the lead field matrix (LFM). This relationship is determined by first solving the forward problem for all cortical sources. The forward problem determines the electrode potential distribution for a given electromagnetic source.

In order to solve both the forward and inverse problems, an electrical model must be incorporated for both the electromagnetic source and the head volume conductor. The source model used in this thesis is the dipolar model and the realistic head model is constructed from MRI by the finite volume method (FVM, Rosenfield et al., 1996; Neilson et al., 2005)

### **2.3.1 Source Model for the Inverse Problem**

As explained in section 1.3.2, the bioelectric source of the measured EEG signal is a group of synchronously active pyramidal cells within the cortical layer of the brain. At large distances compared to dimensions of the pyramidal cells, the measured potential difference is equivalent to that generated by a dipole (Nunez, 1981). This is the case for potential distribution detected by the scalp EEG. Thus, the source of the EEG signal is modelled by a current dipole.

It is imperative to recognize that the current dipole is not actually a real physical element in the cortex, but it is a representation of the activity of a group of pyramidal cells. The dipole represents the center of gravity of volume of current. For activity over an extended area of the cortex, a collection of dipoles can be used as the source model.

### **2.3.2 Head Model for the Inverse Problem**

The volume conductor model defines both the geometric and electromagnetic properties of the head. The mathematical description of the volume conductor is used to calculate the scalp potential distribution due to the activity of the dipolar sources. This is termed the solution to the forward problem.

The earliest head models used to solve the forward problem were spherical volume conductors, with concentric shells representing gray matter, skull, and scalp tissue (Kavanagh et al., 1978). The advantage of this type of model is that the relationship between source activity and scalp potential can be analytically determined. However, it has been shown that this model is too simplistic for most clinical applications, especially for more critical situations such as EEG source localization for epilepsy research (Ebersole, 1997; Cuffin et al., 2001). The geometry and conductivity of the various

tissues in a patient's head affect the scalp potential measured by electroencephalograms (Cuffin, 1993; Haueisen et al., 1997; Ramon et al., 2004). Thus, a more realistic head model created from magnetic resonance images is essential for EEG source analysis.

Numerical methods are necessary for solving the forward problem for realistic head models. One technique is the boundary element method (BEM) (Hämäläinen and Sarvas, 1989; Fuchs et al., 2001). In this approach, tissue boundaries taken from segmented magnetic resonance images are tiled as discrete triangular elements. Although the BEM is a more geometrically accurate head model than the spherical model, it cannot account for holes in tissue boundaries such as the skull or for anisotropic conductivity in tissues such as skull or white matter.

A technique that can account for both tissue boundary holes and anisotropic tissue conductivity is the finite element method (FEM) (Miller and Henriquez, 1990; Rosenfeld et al., 1996; Buchner et al., 1997). This method discretizes the entire head into finite volumetric elements. Restrictions on the element size, smoothness, and inter-compartment distance ensures the stability of this type of realistic head model, but makes it more complex to generate (Michel et al., 2004). In addition, many volumetric elements are needed to incorporate all the details of a patient's head, leading to high computational demands when solving the forward problem.

An alternative is to discretize the head directly from the volume elements (voxels) of the MRI. This can be accomplished by using the finite volume method (FVM, Rosenfeld et al., 1996; Neilson et al., 2005), which centers the cubic voxels onto nodes placed on a regular Cartesian grid. This model is equivalent to a three-dimensional mesh circuit with Kirchhoff's Current Law applied to each node (Neilson et al., 2005). The

advantage of this method is that since the elements are the same dimensions as the voxels, mesh generation is simpler than for the finite element method.

### 2.3.2.1 Lead Field Matrix

To solve the inverse problem, the relationship between neural source activity and electrode potential distribution first needs to be determined. This relationship is mathematically represented by the lead field matrix (LFM). Specifically, multiplying the LFM with an estimated source current density vector gives the potential values at the scalp electrodes. Determination of the LFM depends only on the volume conductor model and the electrode distribution.

The traditional method for constructing the LFM is to compute the potential at the electrodes for each dipolar source of unit strength, in each of the orthogonal directions. This would correspond to computing  $(N \times 3)$  forward solutions, where  $N$  is the number of sources in the cortex. However, the reciprocity property of linear volume conductors simplifies the forward problem calculations needed to determine the LFM. The reciprocity principle states that the potential difference between electrodes  $A$  and  $B$  due to a dipole source is equivalent to the dot product of the dipole source moment,  $\mathbf{d}$ , with the electric field,  $\mathbf{E}$ , generated at the dipole location by a unit current injected between the two electrodes:

$$\Phi_{AB} = \frac{-(\mathbf{E} \cdot \mathbf{d})}{I_{AB}} \quad (1)$$

where  $\Phi_{AB}$  is the potential measured between electrodes  $A$  and  $B$  and  $I_{AB}$  is the magnitude of current injected at electrode  $A$  and removed at electrode  $B$  (Plonsey, 1963;

Rush and Driscoll, 1969). Therefore, if a unit current is used, the lead field for each dipolar source is simply equivalent to the electric field produced at that location.

For each electrode site, the lead field is calculated by first placing a unit current source at the electrode site and a current sink at the reference electrode. The forward problem is then solved for potentials everywhere within the volume conductor model. The gradient of the computed potential field at the dipolar source locations gives the corresponding electric field vector  $\mathbf{E}$ . With a unit current source injected at each electrode site, the lead field is equivalent to this electric field.

### **2.3.3 Source Localization Methods**

There are two different approaches to solving the inverse problem: dipolar models or distributed source models. The basic assumption for dipolar models is that a small number of sources can account for EEG measurements, with fewer dipolar sources than the number of electrodes used to measure the signal (overdetermined inverse problem). Alternatively, the distributed source models use a great deal more dipolar sources than the number of electrodes used to measure the signal (underdetermined inverse problem). The overdetermined dipolar model cannot uniquely fit all the EEG data, but can determine a unique source configuration in a least squares fashion. On the other hand, the underdetermined distributed source model has an infinite number of source configurations that can account for the same measured potential distribution. Therefore, *a priori* information needs to be introduced into the inverse problem to be able to find an “optimal” solution.



### 2.3.3.1 Dipolar Models

The idea behind dipolar model source localization is to compare the computed scalp potential from a small group of dipoles placed at a given location and orientation to the measured scalp signal. The computed potential from the forward model is compared to the measured potential by calculating the squared error. Usually, the dipolar configuration with minimum squared error is accepted as the solution to the inverse problem: this is the least-squared source estimation.

An exhaustive search of all possible dipole locations and orientations is computationally demanding, especially if more than one dipole is involved in the configuration. Instead of performing an exhaustive search, directed search algorithms have been developed with the intention of reducing the computational load (Khosla et al., 1997; Uutela et al., 1998). A risk with these methods is the algorithms become trapped in local minima and thus cannot locate the global minimum.

The simplest form of source localization using the dipolar model is the instantaneous single moving dipole. This method models the neural source as a single dipole with a specific orientation and location at a single point in time. The dipole moves in orientation and location as the measured potential changes with time. This technique has been applied to epileptiform potentials. It is an adequate model only if the neural source is small and geometrically simple, the propagation of the source in the cortex is not complex, and the propagation ends before repolarisation occurs at the original source location (Ebersole, 1997). Often, epileptic activity will have several simultaneous sources throughout the brain, which cannot be modelled by this technique. Spatiotemporal multiple dipole modelling considers both the spatial and temporal components of the

dipolar model, thus taking into account overlapping activity from several sources (Sherg and Von Cramon, 1986; Scherg, 1992). This method fixes the dipole orientation and location of the dipoles while varying the strength and polarity over time.

The difficulty with using dipolar models is determining beforehand the correct number of sources needed for the inverse problem. If the estimated number of sources is incorrect, it is expected that the assumed locations of the sources are also incorrect. Different mathematical techniques have been developed in an attempt to estimate the number of active sources *a priori* to improve on the source localization accuracy (Mosher et al., 1992; Koles and Soong, 1998).

### **2.3.3.2 Distributed Source Models**

Instead of trying to determine the number of neural sources beforehand, distributed source models set up a solution space with a fixed number of dipoles much greater than the number of electrodes. Only the orientations and strengths of these dipoles vary with time, simplifying the equations for distributed inverse solutions to a linear format.

The inverse solution for distributed source models is the configuration of current activity in the solution space that best describes the EEG signal. To solve the underdetermined inverse problem of distributed source models, constraints from *a priori* information need to be introduced. Different techniques have been developed which use mathematical, physiological, structural imaging, and/or functional imaging information. Regularization parameters are also introduced into the inverse problem to account for noise in EEG signals, providing stability so that small variations in the data due to noise do not propagate as large errors in estimated source configuration.

One popular method for source localization, especially if no other *a priori* information is available, is the Minimum Norm (MN) solution (Hämäläinen and Illmoniemi, 1994). This method uses the mathematical assumption that the correct current distribution in the source space has the least amount of energy, solving for the current distribution with the minimum L2-norm. This method favours superficial sources because dipoles situated closer to the electrodes require less energy to provide a particular surface potential distribution than dipoles deeper in the cortex.

Weighted Minimum Norm (WMN) solutions attempt to compensate for the depth bias of MN solutions. The simplest weighting strategy is a normalization of the lead field matrix (Lawson and Hanson, 1974). An alternative strategy termed FOCUSS (Focal Underdetermined System Solution, Gorodinsky et al., 1995) recursively determines the weights based on the solution estimated from the previous step. The result is a more focalized solution than typical distributed inverse problems. However, due to the focalized nature of this method, if the electric activity is extensive, as is the case for some epileptic seizures, the FOCUSS solution provides less reliable estimates than other distributed source methods (Gorodinsky et al., 1995).

Another popular distributed source inverse method is Low Resolution Brain Electromagnetic Tomography (LORETA, Pascual-Marqui et al., 1994). This method adds a Laplacian weighting to the Weighted Minimum Norm solution, finding the smoothest possible 3-dimensional current distribution by minimizing the Laplacian of the weighted sources. The solution produces a blurred image of a point source because of the smoothness constraint, but conserves the location of the source (Pascual-Marqui et al., 1994). The physiological rationale for this constraint is that neighbouring pyramidal cells

are simultaneously and synchronously active. Researchers have debated this rationale, since the scale of smoothness of the solution is much larger than the scale of neighbouring neurons (Pascual-Marqui., 1995). However, when compared to the Minimum Norm and Weighted Minimum Norm methods, LORETA has been shown to provide more consistent source localization results (Pascual-Marqui., 1999).

## Chapter 3

### Accuracy of Inverse Source Localization

#### 3.1 Lead Field Matrix Accuracy

It has been shown that a spherical head model is too simplistic for EEG source localization for epilepsy research (Ebersole, 1997; Cuffin et al., 2001). Instead, a realistic patient-specific head model developed from MRI is a more feasible alternative. However, source localization errors still occur if inaccurate or limited information about the lead field matrix parameters are available. Specifically, inaccuracy in the geometric and electromagnetic properties of the head and in the electrode positions on the scalp of the head can propagate as errors in the inverse problem, leading to inaccurate estimations of neural source locations.

One common area of concern is the correct positioning of electrodes on the head model (Khosla et al., 1999; Wang and Gotman, 2001; Michel et al., 2004). The locations of the electrodes on the scalp need to be identified for the inverse problem calculations. Ideally, the exact patient-specific locations of the electrodes should be determined either by MRI-visible localizing markers (Wang et al., 1996) or by a 3D digitizer (Towle et al., 1993). However, these electrode-positioning identification techniques are not always clinically available. As an alternative, the standard 10-10 electrode placement system identifies landmark locations in order to reconstruct approximate electrode positions on the head model. This introduces inaccurate electrode locations and, in turn, source localization errors. However, it has been shown that source localization errors caused by

misplaced electrodes may be negligible compared to errors caused by the noise in the measured EEG signals (Khosla et al., 1999; Wang and Gotman, 2001). Therefore, it may be feasible to use the 10-10 placement system in order to approximate the electrode locations.

The number and distribution of electrodes on the scalp may also affect the accuracy of the inverse problem. Michel et al. (2004) studied the effect of EEG distribution on source localization and demonstrated that if electrodes sample only a portion of the scalp, the inverse problem produces erroneous results. However, it has also been shown that the electrode distribution may be non-uniform as long as it samples the entire head (Benar and Gotman, 2001). Therefore, if a limited number of electrodes are available for source localization, it may be possible to concentrate the electrode distribution in regions with the greatest potential difference.

For volume conductor models produced by segmented MR images, the accuracy of the head model is limited by the amount of information available from the MRI. In a typical clinical setting, only T1-weighted MR images are available for segmentation, which have no distinct delineation between cerebrospinal fluid (CSF) and skull tissue. CSF is a water-like fluid that protects the brain and spinal cord, providing a cushion between the brain and the skull. The reason there is no distinct delineation in T1-weighted magnetic resonance images is tissues with low proton density such as bone and tissues with high water content such as CSF both appear dark on T1-weighted MR images. There are other MRI acquisition techniques, such as proton density and T2-weighted, which have a distinct boundary between CSF and skull, but they have poor contrast between other cephalic tissue types. Therefore, although there is improved

contrast between CSF and skull with these MR images, segmentation between other cephalic tissues will be difficult to perform.

In the past, researchers excluded the CSF layer from the head model since it was could not be easily segmented with T1-weighted MRI. However, Ramon et al. (2004, 2006) demonstrated that including this CSF layer in the head model is essential for accurate source localization results. Furthermore, due to the skull's low conductivity, inaccurate modelling of skull thickness has a strong influence on EEG source localization results (Cuffin, 1993; Hauesien et al., 1997; Ramon et al., 2004; Ramon et al., 2006). Thus, the CSF tissue needs to be included in the head model, and the effect of the CSF segmentation errors on localization accuracy should be studied.

The effect of precise conductivity values for the various tissues in the head model has also been investigated and determined to influence scalp potentials (Haueisen et al., 1997; Awada et al., 1998; Haueisen et al., 2002; Gencer and Acar, 2004; Ramon et al., 2004). There are significant variations in estimations of the conductivity properties of the different tissues, especially for the skull (Geddes and Baker, 1967; Oostendorp et al., 2000; Gonçalves et al., 2003a; Gonçalves et al., 2003b; Lai et al., 2005). This is because there is no direct, reliable method to measure the conductivity properties of a patient's head. Nonetheless, only the relative strengths of the localized sources are typically of interest, and it can be shown that this only requires the skull-to-brain conductivity ratio. Until recently the skull-to-brain ratio was commonly accepted as 1/80, but the latest measurements have shown that this ratio is closer to 1/15 (Oostendorp et al., 2000; Gonçalves et al., 2003 a, b; Baysal and Haueisen, 2004; Lai et al., 2005). Such a large discrepancy in the conductivity ratio may affect the source localization results. Therefore,

the inverse source solutions for varying skull-to-brain conductivity ratios were compared in this study.

Including the realistic anisotropic conductivity properties from cephalic tissues such as white matter may also affect the accuracy of source localization (Haueisen et al., 2002, Wolters et al., 2006). Anisotropy in white matter is attributed to the fibre bundles in this type of tissue, with conductivity greater in the direction of the fibre tract (Geddes et al., 1967). This gives a conductivity ratio of 1:9 for directions normal and parallel to the white matter fibres, respectively (Nicholson, 1965). The anisotropic conductivity of tissue can be deduced from diffusion tensor magnetic resonance images (DTI, Tuch et al., 2001).

It has been shown that white matter tissue anisotropy has a major influence on the forward calculation results, and should therefore affect the accuracy of the inverse problem (Haueisen et al., 2002, Wolters et al., 2006). Currently, the FVM developed by Neilson et al. (2005) cannot incorporate generalized anisotropic information. Thus, we performed a preliminary analysis of the effect of orthotropic white matter conductivity on the accuracy of source localization.

In summary, the following may affect source localization accuracy:

- location of electrodes on the scalp of the head model;
- distribution of electrodes across the scalp;
- definition of the boundary between CSF and skull;
- skull-to-brain conductivity ratio in the head model; and
- white matter orthotropic conductivity in the head model



In this work, the effect of changing these properties of the lead field matrix is studied for a LORETA-like inverse problem.

## **3.2 *a priori* Information**

To deal with the non-uniqueness of the distributed sources (underdetermined) inverse problem, *a priori* information needs to be integrated into the problem. In this study, two different constraints were incorporated into the LORETA algorithm, and their effects on the accuracy of source localization studied. The constraints are to:

- restrict the orientation of the dipolar sources to be normal to the cortical surface; and
- include information from functional imaging modalities such as SPECT

### **3.2.1 Normal Dipolar Source Orientation**

Rather than allowing the dipoles to rotate freely, the dipole orientation can be set normal to the cortical surface. The physiological basis for this constraint is that the majority of pyramidal cells, the neuronal sources of measured scalp potentials, have a columnar organization orientated perpendicular to the cortical sheet (Nunez, 1981). This is a common constraint in linear inverse methods (Dale and Sereno, 1993; Liu et al., 1998; Liu et al., 2002; Phillips et al., 2002a; Lin et al., 2006). Recently, Lin et al. (2006) studied the effect of cortical orientation constraints on the accuracy of various inverse techniques, but did not study the effect on the LORETA inverse method.

### **3.2.2 Functional Imaging Information**

Source location information from functional imaging modalities such as functional MRI (fMRI) and Single Photon Emission Computed Tomography (SPECT)

can also be incorporated into the inverse problem. The rationale for utilizing functional constraints is that the blood flow measured by functional imaging is closely linked to the neural activity measured by EEG (Jezzard et al., 2001). EEG signals have excellent temporal resolution but limited spatial resolution due to the limited number of measurement sites and the volume conduction effect (Nunez, 1981). The spatial resolution can be improved upon by using functional imaging information as a spatial constraint in the inverse problem.

Functional MRI provides an indirect non-invasive measurement of variations in neural metabolic activity. When neurons are activated, there is an increase in metabolism followed by an increase in surrounding cerebral blood flow. This alters the ratio of oxygenated to deoxygenated blood in the local blood vessels, which in turn changes the magnetic state of haemoglobin and creates local alterations in the MR signal (Jezzard et al., 2001). Functional MRI measures this blood-oxygenation-level-dependent (BOLD) response. fMRI has relatively high spatial resolution, but its temporal resolution is limited by the delay of the hemodynamic response (Jezzard et al., 2001).

Although fMRI-weighted source localization is a popular research area (Liu et al., 1998; Dale et al., 2000; Gonzalez Andino et al., 2001; Jezzard et al., 2001; Wagner and Fuchs, 2001; Phillips et al., 2002a; Babiloni et al., 2003; Gotman et al., 2006; Liu et al., 2006), fMRI acquisition for epileptic patients is not always clinically available and is impractical for some ictal events. An alternative functional imaging technique that is frequently used for clinical epilepsy diagnosis is SPECT. This imaging modality also measures blood flow changes, but with a lower spatial resolution. The advantages of

SPECT are that it can measure ictal as well as interictal events and it is already currently used in a clinical setting for epileptic patients.

SPECT images are formed from measuring the photon emission from radiotracers intravenously injected and trapped within the brain for an extended period, creating a “snapshot” of cerebral blood flow as it was during injection (Henry et al., 2000). During ictal events, blood flow increases in the epileptogenic region (focal hyperperfusion) while during interictal events, some patients show decreased blood flow (focal hypoperfusion). To identify perfusion changes, ictal SPECT images are compared to baseline interictal images by using the technique termed SISCOM (Subtraction Ictal SPECT Coregistered to MRI) (O’Brien et al., 1998, 1999), as shown in Figure 3. Researcher So (2000) demonstrated that for a group of patients whose epilepsy was difficult to localize with only MRI and EEG, SISCOM improved source localization, with a sensitivity of 88% compared to 64% for ictal EEG.

There is no simple relationship between increased neural activity measured by EEG and increased cerebral blood flow measured by SPECT/fMRI (Logothetis et al., 2001). Since EEG and SPECT/fMRI measure different physical aspects of brain function, there may be differences in the location and/or extent of foci shown by each method. The uncertainty in source localization from EEG measurements is due to the imprecision of the volume conductor model and the ill-posed nature of the inverse problem. On the other hand, uncertainty from SPECT/fMRI information is from the discrepancy between the measured signal and the actual neural activity location as well as the lack of understanding of the relationship between neural activity and blood flow (Logothetis et al., 2001). In addition, false localization may occur in SPECT if the radiotracer is injected

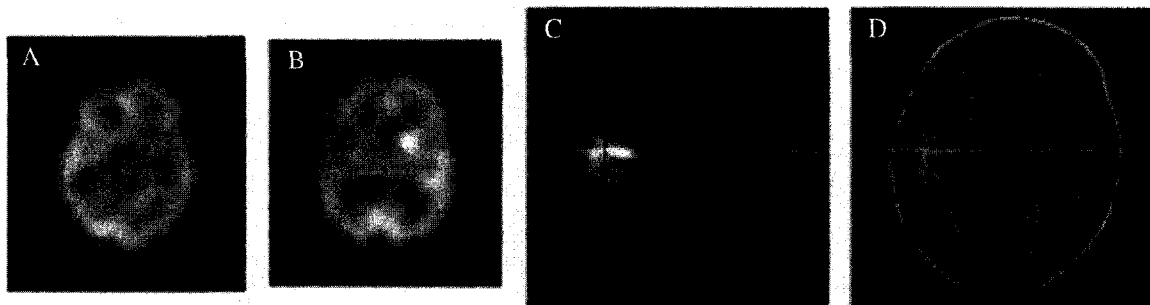


**Figure 3 Example SPECT and SISCOM images from a patient.** Ictal (A) and interictal (B) SPECT images can be combined using subtraction ictal SPECT (SISCOM) (C) with magnetic resonance images (MRI) (D) to show a hyperperfusion area in the right frontotemporal region. Kaiboriboon et al, 2002

after the seizure has already spread to distant locations from the epileptogenic zone (So, 2000). Due to these uncertainties between the EEG and SPECT/fMRI signals, functional imaging information is best used as a soft constraint for source localization (Liu et al., 1998; Dale et al., 2000; Gonzalez Andino et al., 2001; Wagner and Fuchs, 2001; Phillips et al., 2002a; Babiloni et al., 2003; Liu et al., 2006)

## Chapter 4

# Setup of Head Model and Inverse Problem

### 4.1 Realistic Head Model from MRI

We constructed a finite volume head model from segmented MRI slices of an adult female epileptic patient. The slices are T1-weighted with 1x1x1 mm sized voxels, 228x171 in-plane resolution, and 176 continuous slices. The total number of voxel elements used for the FVM was over two million. The head was segmented using segmentation software termed mtrack (Withey, 2006) into seven different tissue types: scalp, fat and muscle, skull, CSF, gray matter, cerebellum and pons, and white matter. The segmentation method used is a statistically based edge tracing method that utilizes the Kalman filter (Withey, 2006). Although this semiautomatic technique can provide very detailed segmentation results, the method is user-dependent. Therefore, there is a correlation between the amount of time a user spends on each MRI slice and the level of segmentation detail, as illustrated in Figure 4. For this study, a compromise between user

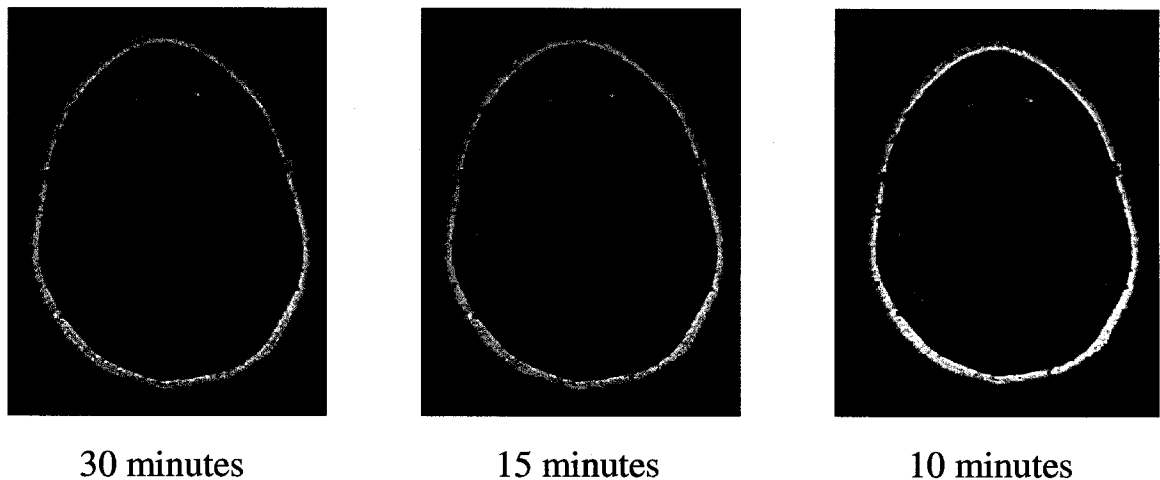


**Figure 4 Segmentation results for a single MRI slice using mtrack tool.** The more user input into the segmentation program (corresponding to more time for processing) is consistent with more detailed segmentation results.

input and segmentation details was used, which corresponds to segmentation results similar to those shown in the middle image of the Figure.

The largest difficulty in segmenting MR images with the mtrack technique is that the CSF-skull boundary is not easily discernible in T1-weighted MRI. This is illustrated in Figure 5B, a blown-up image of the bottom left corner of the same MRI slice as shown in Figure 5A. Instead of using the user-dependent edge-based mtrack method, an initial approximation of the CSF-skull boundary was obtained from the FMRIB Software Library's (FSL) automated tools BET (Brain Extraction Tool, Smith, 2002) and FAST (FMRIB's Automated Segmentation Tool, Zhang et al., 2001). These tools are completely automated pixel-classification segmentation techniques. The automated BET tool is first applied to 3D MR images in order to separate the brain tissue (CSF, grey, and white matter) from the surrounding tissues. This tool employs a deformable model that uses a set of locally adaptive model forces in order to fit to the brain surface. The brain tissue is then further segmented into CSF, grey, and white matter with the FAST tool, which utilizes a hidden Markov random field model and statistical clustering.

Figure 5C shows the same horizontal slice as Figure 5A for the initial approximation of the segmented CSF tissue class as obtained from FSL software. The segmented CSF tissue was then cleaned by removing isolated pixels and by morphologically closing the surface with a spherical structuring element in order to remove small holes, as shown in Figure 5D & E. Because the CSF surface was determined by a different segmentation method than the remainder of the tissues, the two different segmentation results needed to be combined. Specifically, the segmented cortical sheet overlapped with the approximated CSF layer, as shown in Figure 5E. This

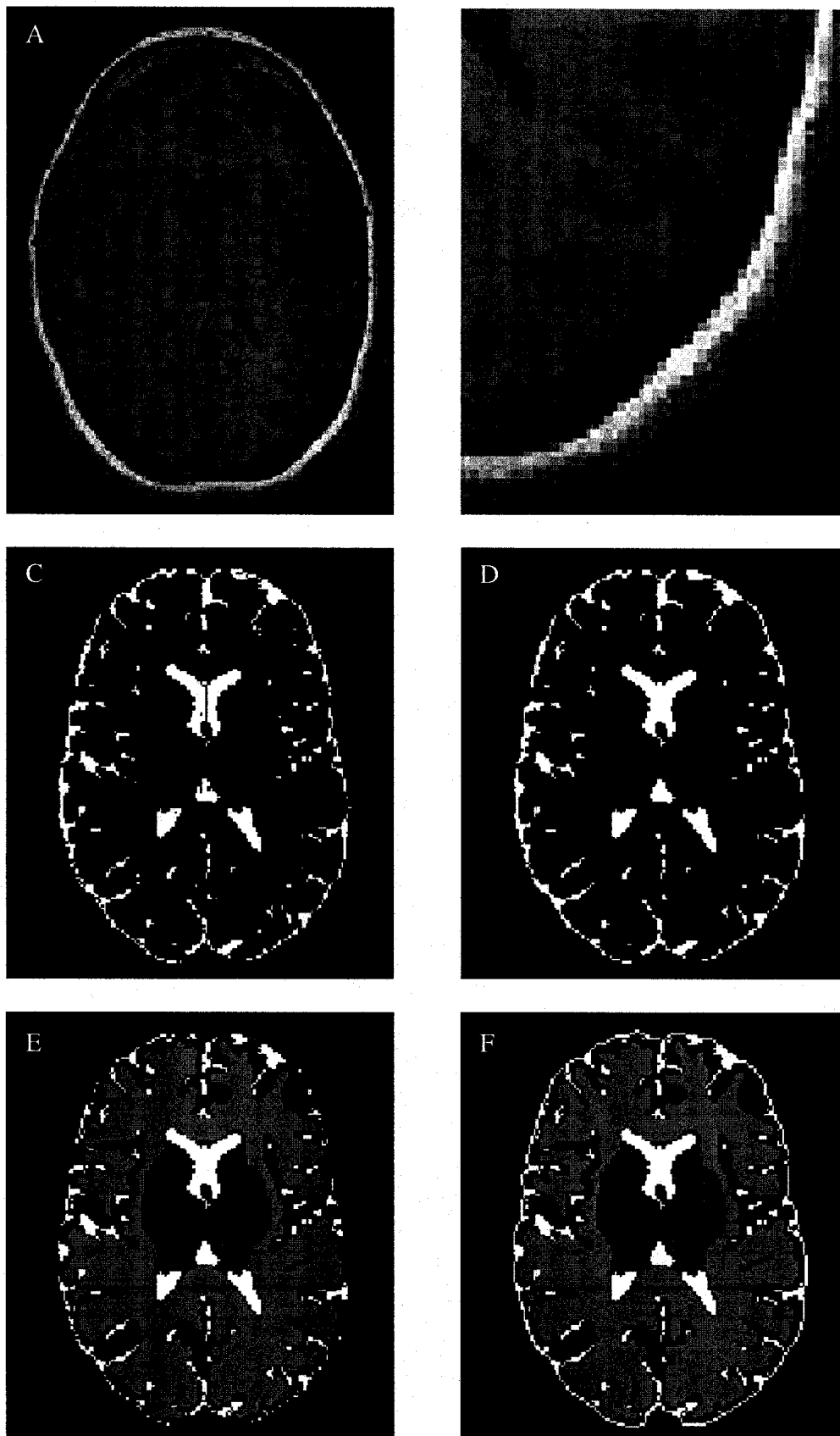


**Figure 5 Segmentation of CSF tissue in MRI.** A) Slice of MRI from a patient. The CSF/Skull boundary is difficult to delineate in T1-weighted images, as shown in (B). The initial segmentation of the CSF is shown in (C), with the cleaned version in (D). When this is added to the outside of the segmented cortical sheet (E), the CSF is not a closed surface. Therefore, this CSF tissue is expanded slightly to the final segmented image shown in (F) (tissues grey matter, white matter, and CSF shown)

is unrealistic, since the cortical surface should be surrounded by protective cerebrospinal fluid. Therefore, the final step in defining the CSF-skull boundary was to ensure the cortical surface was surrounded by cerebrospinal fluid tissue. This was accomplished by setting all pixels connected to the outer cortical boundary as CSF tissue, as shown in Figure 5F.

The combined segmentation results for all the tissue types and for the same MRI slice are shown in Figure 6. The resistivity values assigned to the various tissue classes are given in Table 1. These values were derived from literature (Geddes and Baker, 1967; Foster and Schwan, 1986; Ferree et al., 2000; Gonçalves et al., 2003 a, b; Baysal and Haueisen, 2004). The skull-to-brain ratio of 1/15 was obtained from the most recent measurements in literature (Gonçalves et al., 2003; Baysal and Haueisen, 2004; Lai et al., 2005).

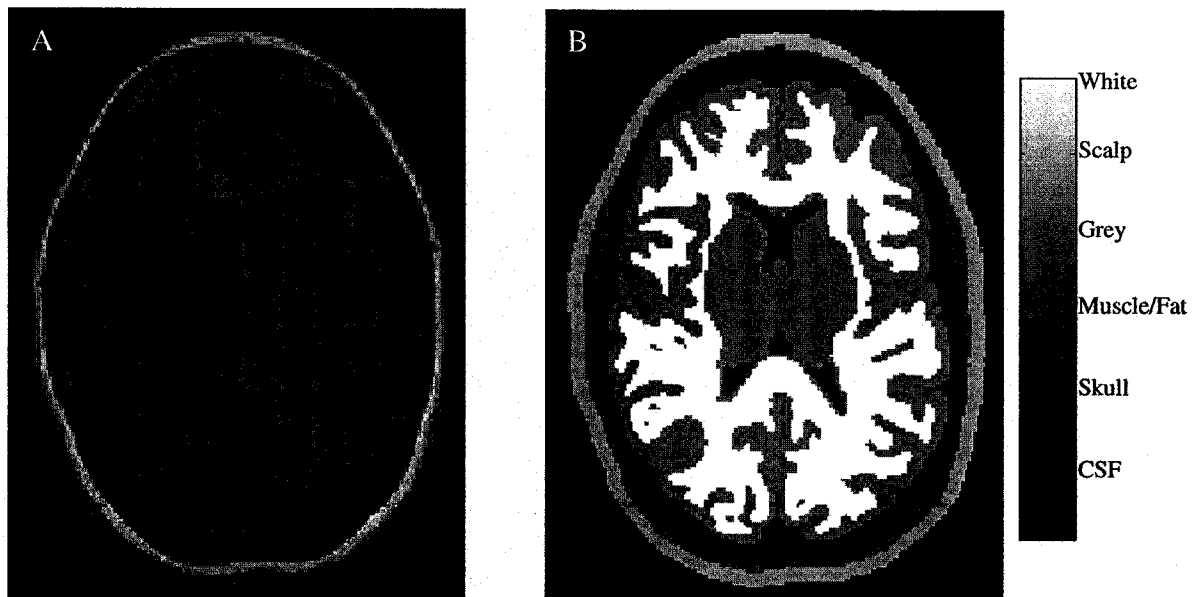


**Figure 6 Final MRI Segmentation Result.** A) Horizontal slice of patient's T1-weighted MR image. The final segmentation result for this slice is shown in B)



**Table 1 Resistivity values of segmented tissue.** Values were derived from literature for the seven different segmented tissue types in the volume conductor model.

Tissue Type	Resistivity ( $\Omega\text{m}$ )	Reference
Scalp	2.75	Geddes and Baker, 1967; Ferree et al., 2000;
Fat and Muscle	15	Ferree et al., 2000;
Skull	45	Gonçaves et al., 2003; Baysal and Haueisen, 2004; Lai et al., 2005
CSF	0.65	Geddes and Baker, 1967
Gray Matter	3	Geddes and Baker, 1967; Foster and Schwan, 1986
Cerebellum and Pons	3	Geddes and Baker, 1967; Foster and Schwan, 1986
White Matter	7	Geddes and Baker, 1967

### 4.1.1 Setup of Solution Space

Before defining the grey-matter solution space, the inner and outer surfaces of the segmented cortex were smoothed using a linear Savitzky-Golay filter (Rajagopalan and Robb, 2003). This was done to reduce the noise in the segmented surfaces caused by the limited resolution of the model and by errors introduced from segmentation and surface reconstruction processes. A Savitzky-Golay filter was used to preserve higher moments, in order to maintain edges while still removing noise from the surface. The Savitzky-Golay filter is a linear finite impulse response (FIR) filter, which replaces each data value  $f_i$  by a linear combination  $g_i$  of itself and its surrounding neighbours:

$$g_i = \sum_{n=-n_L}^{n_R} c_n f_{i+n} \quad (2)$$

where  $c_n$  is the filter coefficients for  $n_L$  points to the left of the data point  $i$  and  $n_R$  points to the right of the data point  $i$ . The simplest filters approximate the underlying function within the filter window by a constant value, but a filter such as Savitzky-Golay preserves higher moments by least squares fitting a polynomial of higher order to all

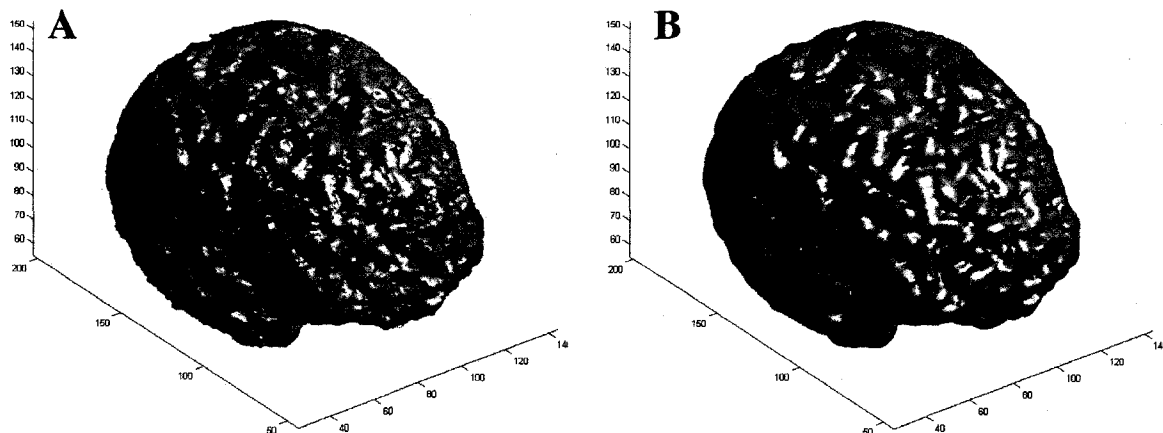


**Figure 7 Smoothing the cortical surface.** (A) Original segmented outer cortical surface and (B) smoothed cortical surface using the Savitsky-Golay filter

points in the window. The output of the filter  $g_i$  is then set to the value of the polynomial at position  $i$ . The effects of this filter for the segmented cortical surface are shown in Figure 7. The number of neighbours for the filter was empirically chosen as two points to the left and right ( $n_L$  and  $n_R$ , respectively). In order to smooth the surface, this filter was applied in all 3-dimensions instead of only in 1-dimension. The Savitzky-Golay filter not only smoothed noise from the cortical surface, but also preserved the details of the gyri and sulci.

The solution space was defined as a single layer of voxels following the contours of the cortical sheet. In order to model the cortical sources as dipoles, each source in the solution space needed to be defined across three voxels of grey matter. This enabled modelling the separation of charges inherent in the dipolar sources. Thus, only voxels surrounded by grey matter were selected as the center of a dipolar source within the single-layer solution space. In order to keep only voxels with surrounding grey matter while also following the contours of the cortical sheet, the solution space was defined along a median surface in between the outer and inner surface boundaries of the grey

matter. The median surface was found by calculating a Euclidean distance map from the outer white matter boundary across the cortical sheet towards the outer grey matter boundary, and then finding the median distance from the inner to the outer surface. Then, only the voxels along this median surface that were surrounded by grey matter in each orthogonal direction were kept as dipolar sources in the solution space.

The average Euclidean distance between solution voxels was less than 2mm, with the maximum distance only 5mm. The total number of voxels in the cortex defined as dipolar solution points was 61,041. The solution space can also be expanded to include the full cortex instead of a single layer. Although such a solution space may provide a more detailed depiction of neural activity, the number of solution points more than doubles, increasing the memory requirements for inverse calculations.

#### **4.1.2 Electrode Locations on the Head Model**

The voxel locations of the electrodes on the scalp of the head model were determined using the standard 10-10 coordinate system (Sharbrough et al., 1991). There were 32 electrodes total: the standard 20 electrodes typically used in epilepsy analysis, plus additional electrodes placed in the frontal region of the head. These extra electrodes were included because the epilepsy patient was assumed to have frontal lobe epilepsy. The electrode locations on the head model are illustrated in Figure 8.

In order to locate the voxels on the head model's scalp corresponding to the electrode positions, the center of the head model was first calculated by determining the best-fit sphere to the scalp surface. We approximated the center coordinates of the head surface by minimizing the mean squared error with respect to the center point coordinates  $(x_c, y_c, z_c)$  and radius  $(r)$  of a sphere:

$$\text{MSE} = \sum_{i=1}^N ((x(i) - x_c)^2 + (y(i) - y_c)^2 + (z(i) - z_c)^2 - r^2) \quad (3)$$

with the sum over the  $N$  different Cartesian coordinates of the head surface.

The patient's MRI was only segmented to the eye mid-line instead of to the bottom of the head, which leaves a scalp surface that is only a half-spherical shape instead of a full spherical shape. Thus, the  $z_c$  coordinate calculated from equation 3 was manually adjusted to line up with the appropriate bottom transverse plane of the 10-10 coordinate system. This plane includes electrodes  $F_{p1}$ ,  $T_7$ ,  $O_z$ , and  $T_{10}$ , as shown in Figure 2. Before locating the bottom transverse plane of the 10-10 system, we first found the intersection site of the estimated nasion, inion, and preauricular points, since these locations are the references that define the coordinate system (Jasper, 1958; Sharbrough et al., 2001). The bottom transverse plane was then set as 18 degrees ( $180/10$ ) above the

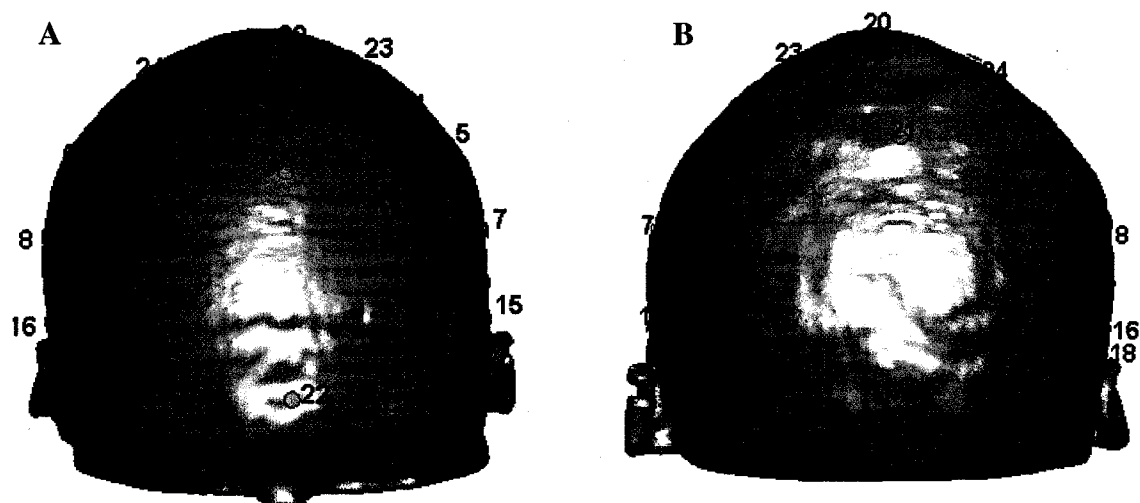


**Figure 8 Electrodes positioned on the scalp surface of the head model.** (A) and (B) illustrate electrode positions for the estimated center coordinate of the head. The red circles represent the standard 20 electrodes typically used in epilepsy research, while the blue circles are the electrodes that were added for more detailed frontal lobe analysis.

plane of the reference points' intersection site, giving the final reconfigured  $z_c$  coordinate (Pascau et al., 2000).

The center coordinates of the head model plus the tip and spin angles defining each electrode position were then used to calculate the voxel coordinates of the electrodes on the scalp of the head model. For each electrode, this was accomplished by projecting a ray from the center point of the model outwards towards the scalp surface, with the angle of the ray corresponding to the spherical coordinates of the electrode. The voxel location closest to the intersection point of the scalp surface with the ray was set as the electrode position for the volume conductor model.

### 4.1.3 Calculation of the Lead Field Matrix

Before solving the inverse problem, the lead field matrix (LFM) needs to be calculated. The LFM maps the relationship between all possible current sources in the brain and the measured electrode potentials on the scalp. As described in section 1.4.2.1, this relationship is determined by solving the forward problem for a current source at each electrode site and a current sink at the reference electrode, for potentials at every node in the solution space.

To model the electric and magnetic fields produced from brain activity, the quasistatic Maxwell equations are used (Plonsey, 1969). The Poisson equation governs the behaviour of the electric field from the neural sources:

$$\nabla \cdot \sigma \nabla \Phi = \nabla \cdot \vec{I}_i \quad (4)$$

where  $\sigma$  is the conductivity of the volume ( $\Omega\text{m}^{-1}$ ),  $\Phi$  is the electric potential, and  $\vec{I}_i$  is the source current density ( $\text{A}/\text{m}^2$ ) (Plonsey, 1969). Discretization of Poisson's equation using

the FVM developed by Neilson et al. (2005) leads to the following equation for each voxel in the head model

$$\sigma_{eff1}(\Phi_1 - \Phi_0) + \sigma_{eff2}(\Phi_2 - \Phi_0) + \dots + \sigma_{eff5}(\Phi_5 - \Phi_0) + \sigma_{eff6}(\Phi_6 - \Phi_0) = \frac{I_0}{h} \quad (5)$$

where  $\Phi_0$  is the potential at the center node,  $\Phi_n$  is the potential at each neighbouring node,  $\sigma_{effn}$  is the conductivity between the center node and each adjacent node,  $I_0$  is the total current flow into the center node, and  $h$  is the edge length of each voxel. Most nodes have a current  $I_0$  equal to zero, except for if a current sink or source is located at the node. Each voxel in the solution space is centered on a node coupled to six adjacent nodes via resistors, as shown in Figure 9. The effective conductivity between two nodes is simply the series combination of the conductivities of the two adjacent half-voxels. For example, the effective conductivity between the nodes centered at voxels 0 and 1 from Figure 9 is

$$\sigma_{eff1} = \frac{2\sigma_0\sigma_1}{\sigma_0 + \sigma_1}. \quad (6)$$

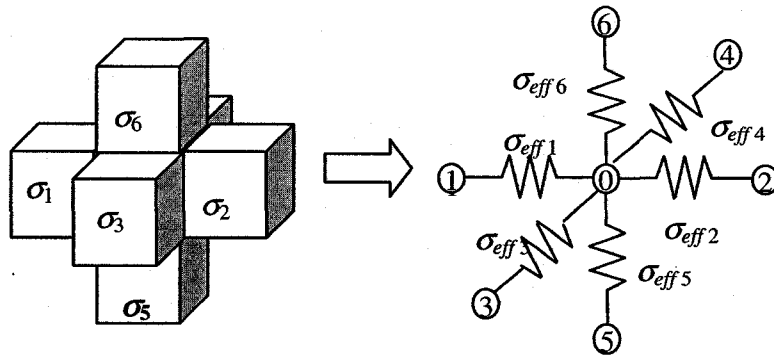


**Figure 9 Finite Volume Method.** A set of adjacent voxels modelled as nodes in a 3D mesh circuit. A node linked to six neighbouring nodes by resistors characterizes each voxel.

Applying Eq. 4 to every node in the source space leads to a system of equations governed by Ohm's law that can be represented in matrix-vector form

$$\mathbf{A}\Phi = \mathbf{I}_0 \quad (7)$$

where  $\mathbf{A}$  is the tissue conductivity matrix,  $\Phi$  is a column vector of nodal potentials, and  $\mathbf{I}_0$  is a column vector of unit nodal current sources and sinks. The forward problem is then solved for the potential differences,  $\Phi$ , using the conjugate-gradient method (Neilson et al., 2005).

The potential difference at the electrode locations is related to the source current density by the lead field matrix,  $\mathbf{K}$

$$\Phi = \mathbf{K}\mathbf{J} \quad (8)$$

where  $\mathbf{J}$  is the vector of unknown current densities. The LFM was calculated from the forward problem calculations using the reciprocity property of linear volume conductors, as mentioned in Section 1.4.2.1. Specifically, the lead field was calculated for each electrode location and all dipolar sources by solving the forward problem for a unit current source injected at that electrode site and a current sink at the reference electrode. The potential values were extracted at all the nodes within the volume conductor. The electric field at each node of the solution space was calculated as the gradient of the computed electrical potential, which with a unit current source was equivalent to the lead field matrix, as shown in Equation 1.

## 4.2 Inverse Problem

The inverse method we used to localize the sources of the EEG signal is based on the LORETA method (Pascual-Marqui et al., 1994, Pascual-Marqui, 1995). The goal of the inverse problem is to solve the following linear equation for the neural current distribution:

$$\Phi = \mathbf{K}\mathbf{J} + \mathbf{b} \quad (9)$$

where  $\Phi$  is a  $P$ -sized vector of instantaneous EEG recordings,  $\mathbf{K}$  is the lead field  $P \times 3M$  matrix with each row specifying the lead field of a given electrode,  $\mathbf{b}$  is a  $P$ -sized noise vector, and  $\mathbf{J}$  is the  $3M$  vector of unknown current densities.  $M$  refers to the number of dipolar sources in the solution space and  $P$  refers to the number of electrode sites. Each dipole moment is represented by three components placed along the three-dimensional Cartesian coordinate system.

This distributed source inverse problem is underdetermined. Thus, additional constraints are needed in order to obtain a stable and unique solution. For LORETA solutions, an additional constraint included in the inverse problem is that of neighbourhood spatial smoothing. For instantaneous EEG measurements, the discrete solution of LORETA is obtained by solving the following:

$$\min_{\mathbf{J}} \|\mathbf{B}\mathbf{W}_d\mathbf{J}\|^2 \quad \text{under constraint: } \Phi = \mathbf{K}\mathbf{J} \quad (10)$$

The discrete  $3M \times 3M$  matrix  $\mathbf{B}$  implements roughening, which when minimized results in spatial smoothing, while the diagonal  $3M \times 3M$  matrix  $\mathbf{W}_d$  implements depth weighting.  $\mathbf{W}_d$  is obtained by normalizing the three components of the dipole moment of the lead field matrix for each electrode placement. Specifically,  $\mathbf{W}_d$  is equal to:



$$\mathbf{W}_d = \Omega \otimes \mathbf{I} \quad (11)$$

where  $\otimes$  represents the Kronecker product of the diagonal  $M \times M$  matrix  $\Omega$  and  $3 \times 3$  identity matrix  $\mathbf{I}$ . The diagonal elements of  $\Omega$  are obtained by:

$$\Omega_{ii} = \sqrt{\sum_{\eta=1}^P \mathbf{k}_{\eta i}^T \mathbf{k}_{\eta i}} \quad (12)$$

with  $\mathbf{k}_{\eta i}$  equivalent to the lead field vector for electrode number  $\eta$  and source location  $i$ .

In order to deal with noise-contaminated EEG recordings as well as to insure stability, regularization needs to be applied to the inverse problem. In our case, Tikhonov regularization was used, which chooses the solution that solves the minimization problem:

$$\min_{\mathbf{J}} \left\{ \|\Phi - \mathbf{KJ}\|^2 + \alpha \|\mathbf{BW}_d \mathbf{J}\|^2 \right\} \quad (13)$$

The regularization parameter  $\alpha$  provides a compromise between fitting the model and fitting the *a priori* assumptions, the first and second terms of Equation 13, respectively. If the value of  $\alpha$  is too large, the solution is over-smoothed and over-regularized (i.e. – too much information lost in the inverse solution); however if  $\alpha$  is too small, the solution is dominated by noise and under-regularized (i.e. – not enough noise was filtered out). The optimal value of  $\alpha$  was calculated using the L-curve method (Hansen and O’Leary, 1993). The L-curve is a parametric logarithmic plot of the first term of Equation 13 versus the second term. The corner of the L-shaped curve represents a good balance between minimization of the two terms of the equation, and the corresponding regularization value  $\alpha$  for the corner of the curve is optimal for inverse calculations.

The solution to the inverse problem expressed in Equation 13 is:

$$\hat{\mathbf{J}} = \mathbf{T}\Phi \quad (14)$$

where  $\mathbf{T}$  is the  $3M \times P$  transformation matrix, and  $\hat{\mathbf{J}}$  is the estimated current distribution of the cortical sources. The transformation matrix for this underdetermined inverse problem is given by:

$$\mathbf{T} = (\mathbf{W}^T \mathbf{W})^{-1} \mathbf{K}^T \{ \mathbf{K} (\mathbf{W}^T \mathbf{W})^{-1} \mathbf{K}^T + \alpha \mathbf{I} \}^{-1} \quad (15)$$

with  $\mathbf{W}$  equivalent to  $\mathbf{W}_a \mathbf{B}$ .

The transformation matrix in Equation 15 is valid only if  $\mathbf{K} \mathbf{K}^T$  is of full rank, as is the case when the location of the reference electrode is known. The lead field matrix,  $\mathbf{K}$ , can be made reference-independent by centering the LFM with an average reference operator  $\mathbf{H}$ , which references the electrodes to the mean of all recording channels. Applying the average reference operator insures that the net potential summed over the entire surface is zero. The inverse problem in (13) is then consistently described as:

$$\min_{\mathbf{J}} \{ \|\mathbf{H} \Phi - \mathbf{H} \mathbf{K} \mathbf{J}\|^2 + \alpha \|\mathbf{B} \mathbf{W}_a \mathbf{J}\|^2 \} \quad (16)$$

with average reference operator,  $\mathbf{H}$ , equal to:

$$\mathbf{H} = \mathbf{I} - \mathbf{1} \mathbf{1}^T / \mathbf{1}^T \mathbf{1} \quad (17)$$

where  $\mathbf{1}$  represents a  $P \times 1$  vector of ones and  $\mathbf{I}$  the  $P \times P$  identity matrix. With this transformation, the Moore-Penrose pseudo-inverse must be used to calculate the transformation matrix:

$$\mathbf{T} = (\mathbf{W}^T \mathbf{W})^{-1} \mathbf{K}^T \{ \mathbf{K} (\mathbf{W}^T \mathbf{W})^{-1} \mathbf{K}^T + \alpha \mathbf{H} \}^+ \quad (18)$$

with  $\mathbf{K}$  equivalent to  $\mathbf{H} \mathbf{K}$  and  $D^+$  indicating the Moore-Penrose pseudo-inverse of  $D$ .

Typically, for LORETA solutions, the weighting matrix  $\mathbf{B}$  is a Laplacian operator, and the inverse matrix  $\mathbf{B}^{-1}$  then implements a spatial smoothing operator. If the number of dipolar sources in the brain is substantial, which is typically the case for high-resolution

realistic head models, the computational effort to invert the matrix  $\mathbf{B}$  is considerable since it is sparse but not diagonal (Fuchs et al., 1999). An alternative is to use a low-pass spatial smoothing operator directly in the calculation of the transformation matrix  $\mathbf{T}$ , instead of inverting a high-pass Laplacian operator. Thus, the transformation matrix calculated in (18) is equivalent to:

$$\mathbf{T} = (\mathbf{W}_a^{-1} \mathbf{S} \mathbf{S}^T \mathbf{W}_a^{-1}) \mathbf{K}^T \{ \mathbf{K} (\mathbf{W}_a^{-1} \mathbf{S} \mathbf{S}^T \mathbf{W}_a^{-1}) \mathbf{K}^T + \alpha \mathbf{H} \}^+ \quad (19)$$

where  $\mathbf{S}$  is a 3D low-pass spatial smoothing operator.

### 4.2.1 Normal Dipolar Orientation Constraint

With the orientation vector of the dipoles fixed to be normal to the cortical surface, the potentials measured at the electrode sites are now described by

$$\Phi = (\mathbf{KN}) \mathbf{J}_0 \quad (20)$$

where  $\mathbf{J}_0$  is an  $M$ -sized vector of the current density magnitude at each dipole source location in the cortex (Pascual-Marqui, 1995).  $\mathbf{N}$  is a  $3M \times M$  matrix giving the outward normal vector coordinates of each dipole, such that  $\mathbf{J} = \mathbf{N} \mathbf{J}_0$ .

The normal vector orientation can also provide information about the relative positioning of the dipolar sources. Specifically, due to the smooth shape of the cortical sheet, if the angle between two neighbouring dipoles is larger than 135 degrees, it can be assumed that the dipoles are on opposite sides of the sulcus. Therefore, these two dipoles should not be defined as neighbours. This information alters the smoothing matrix  $\mathbf{S}$ , with the spatial operator no longer smoothing the current density of the sources that are on opposite sides of the sulcus.

The solution to the inverse problem with the normal orientation constraint is now given by

$$\hat{\mathbf{J}}_0 = \mathbf{T}_0 \Phi \quad (21)$$

with the transformation matrix  $\mathbf{T}_0$  defined as

$$\mathbf{T}_0 = (\mathbf{W}_d^{-1} \mathbf{S} \mathbf{S}^T \mathbf{W}_d^{-1}) \mathbf{N}^T \mathbf{K}^T \{ \mathbf{K} \mathbf{N} (\mathbf{W}_d^{-1} \mathbf{S} \mathbf{S}^T \mathbf{W}_d^{-1}) \mathbf{N}^T \mathbf{K}^T + \alpha \mathbf{H} \}^+ \quad (22)$$

and  $\mathbf{T}_0$  now an  $M \times P$  size matrix instead of a  $3M \times P$  matrix.

## 4.2.2 Incorporation of SPECT Image Information

Source location information from SISCOM SPECT images is incorporated into the inverse problem by introducing another weighting matrix to the inverse problem, changing the transformation matrix to:

$$\mathbf{T}_0 = (\mathbf{W}_{fd}^{-1} \mathbf{S} \mathbf{S}^T \mathbf{W}_{fd}^{-1}) \mathbf{N}^T \mathbf{K}^T \{ \mathbf{K} \mathbf{N} (\mathbf{W}_{fd}^{-1} \mathbf{S} \mathbf{S}^T \mathbf{W}_{fd}^{-1}) \mathbf{N}^T \mathbf{K}^T + \alpha \mathbf{H} \}^+ \quad (23)$$

The weighting matrix  $\mathbf{W}_{fd}$  is given by

$$\mathbf{W}_{fd} = \mathbf{W}_f \mathbf{W}_d \quad (24)$$

where  $\mathbf{W}_f$  is a diagonal matrix, with a value of 1.0 if there is corresponding SPECT information. The value at source locations with no SPECT activity should be greater than one in order to incorporate SPECT as a soft constraint (Liu et al., 1998; Dale et al., 2000; Gonzalez Andino et al., 2001; Wagner and Fuchs, 2001; Phillips et al., 2002a; Babiloni et al., 2003; Liu et al., 2006).

## Chapter 5

# Computer Simulations and Results

The effects of head model precision and *a priori* constraints were tested with a LORETA-like solution to the inverse problem and analyzed both qualitatively with clinical EEG and quantitatively with validation metrics calculated from randomly placed dipolar sources. To evaluate quantitatively the effects of head model precision and *a priori* constraints on source localization, the inverse problem was calculated for 2500 separate randomly placed dipolar sources. Each change in the volume conductor model or addition of *a priori* constraint was compared to the same Base Model, corresponding to the head model with typical information available from clinical data and no additional constraints as given in Section 2.2.

For each dipolar source, the forward problem was solved for the Base Model using its corresponding lead field matrix to give the potential distribution on the electrodes. The orientation of each source for forward calculations was set to the normal cortical vector direction. The spatial extent of the dipolar source was randomly set to  $1\text{mm}^2$ ,  $1\text{cm}^2$ , or  $6\text{cm}^2$ . Most inverse localization accuracy tests are conducted with  $1\text{mm}^2$  dipoles, but Ebersole (1997) has shown that  $6\text{cm}^2$  should be considered as the minimum source area required to observe spike and sharp waves on the scalp electrodes. The source current density was fixed at  $5\text{nA.m}^2$ , uniform within the source extent.

Before solving the inverse problem, zero-mean Gaussian noise was added to the electrode potentials to give four different levels of signal to noise ratio (SNR): INF (no

noise), 20, 10 and 5 dB. SNR is the ratio of signal intensity to noise intensity, measured on a logarithmic scale. This range of SNR was chosen to correspond to clinical EEG recordings, which have shown signal to noise ratio between 10 and 20 dB for highly synchronized and spatially focused activity such as epileptic spikes (Babiloni et al., 2003). For other motor or cognitive activities, the SNR values are typically 5 dB (Regan, 1989). After adding noise to the EEG signal, the inverse problem was solved using the altered head model or the additionally constrained inverse problem. These results were then quantitatively compared to the Base Model using the validation metrics described in Section 2.3.1.

Qualitative evaluation was performed with clinical EEG data obtained from a patient with frontal lobe epilepsy. The different models were compared to the Base Model by creating a movie of the reconstructed cortical source current density over time. The noisy EEG data was sampled at a rate of 245 samples per second and pre-filtered with a band pass filter with a 1-20 Hz band. The covariance matrix of the pre-filtered signal was then further filtered using singular value decomposition (SVD). Specifically, the SVD of covariance matrix  $\mathbf{C}$  of the pre-filtered signal, which is of size  $P \times P$ , is:

$$\mathbf{C} = \mathbf{U}\mathbf{\Sigma}\mathbf{U}^T \quad (25)$$

where  $\mathbf{U}$  and  $\mathbf{U}^T$  are orthonormal  $P \times P$  matrices and  $\mathbf{\Sigma}$  is a  $P \times P$  diagonal matrix with eigenvalues of  $\mathbf{C}$  along the diagonal of the matrix, in descending order. The  $\mathbf{U}$  matrix contains a series of linearly independent principal component vectors of the pre-filtered EEG, with the first vector representing the most prominent feature of  $\mathbf{C}$ . If the signal to noise ratio is relatively high, as in the case for the pre-filtered EEG signal, then only the first  $s$  columns of the SVD matrices represent the source signals, while the remaining

terms are assumed to represent noisy signals. Thus, the matrices can be split into the signal and noise matrices, with the columns of the new  $\mathbf{U}_s$  matrix termed the signal subspace. Noise can be reduced from the pre-filtered EEG signal by an orthonormal projection of the pre-filtered EEG signal onto this signal subspace:

$$\mathbf{EEG}_{filt} = \mathbf{U}_s \mathbf{U}_s^T \mathbf{EEG} \quad (26)$$

with  $\mathbf{EEG}_{filt}$  equivalent to the pre-filtered EEG matrix with  $P$  electrode sites.

Finally, instead of calculating the source current density (SCD) for each moment in time, the SCD was averaged over nine time-slices:

$$\mathbf{J}_{ave} = \text{sum}(\text{diag}(\mathbf{T}(\mathbf{EEG}_{filt,9})\mathbf{EEG}_{filt,9}^T \mathbf{T}^T)) = \text{sum}(\text{diag}(\mathbf{T}\mathbf{R}\mathbf{T}^T)) \quad (27)$$

with  $\mathbf{EEG}_{filt,9}$  representing the  $P \times 9$  vector of  $\mathbf{EEG}_{filt}$  time-slices and  $\mathbf{R}$  the  $P \times P$  covariance matrix of the  $\mathbf{EEG}_{filt}$  matrix. The sum in (27) is over the three x, y, and z components for the averaged source current density of each dipole, which gives an  $M \times 1$  vector of the mean-squared values. For analysis with the normal orientation constraint, the  $\mathbf{T}$  matrix is replaced with  $\mathbf{T}_0$  from equation 22, and the sum is simplified to one dimension.

We performed the forward problem computations, which in turn were used to calculate the corresponding lead field matrix for the different head models, on 1 GHz Intel Pentium3 parallel processors with 2 GB memory. The forward problem calculation for each individual electrode took approximately 35 minutes. The forward and inverse solutions calculated for the randomly placed dipoles, as well as post-processing and visualizations, were computed using Matlab 7.0 software on a 3.2 GHz Intel Pentium 4 processor with 2 GB memory.

## 5.1 Validation Metrics

A performance metric that measures the accuracy of the inverse problem in reconstructing the source location is localization error (LE) (Pascual-Marqui, 1995). Localization error is measured as the Euclidian distance between the actual current source location and the maximum value of the estimated source current density. For spatial extents greater than  $1\text{mm}^2$ , the center of mass was chosen as the location of the actual current source location.

The center of mass error (CME) may also be calculated to evaluate source localization accuracy. The CME is the distance between the center of mass of the estimated source current density and the center of mass of the actual source current extent (Lin et al., 2006). This performance metric takes into account the source distribution of the inverse solution instead of only the maximum value. Only sources with magnitude moments equal to or greater than 50% of the maximum value were included in the calculation to avoid shift from insignificant background dipolar activity. The error value is equal to:

$$\text{CME} = \text{distance}\left(\frac{\sum_i J_{true}(i) * xyz(i)}{\sum_i J_{true}(i)}, \frac{\sum_i \hat{J}(i) * xyz(i)}{\sum_i \hat{J}(i)}\right) \quad (28)$$

where  $xyz(i)$  is the Cartesian x, y, and z coordinates of dipole  $i$  in the solution space (x coordinate from left to right, y coordinate from posterior to anterior, z coordinate from superior to inferior).  $J_{true}(i)$  is the magnitude of the original simulated source current density and  $\hat{J}(i)$  is the estimated source current density of dipole  $i$ . A larger CME value in comparison to a smaller LE value indicates that the dipolar activity is spread away from the original source position, but the maximum value of current density is still near the



correct location. A larger LE value than CME indicates that there is some activity near the correct location in the cortex, but the highest activity is further from the original source location.

Another assessment criterion used in this study is the degree of focalization (DF), which measures the inverse method's ability to estimate the source within the area of the original source location (Im et al., 2003; Im and He, 2006). The DF is defined as the reconstructed energy of the current vector in the original source area divided by the overall reconstructed energy of the current vector in the solution space.

$$DF = \frac{\sum_{i \in \Theta_a} |\hat{j}_i|^2}{\sum_{i=1}^n |\hat{j}_i|^2} \quad (29)$$

where  $\Theta_a$  represents the neighbourhood of simulated dipolar sources. Again, only dipoles with magnitude moments equal to or greater than 50% of the maximum value are included in the calculation to ensure that background activity does not affect the degree of focalization value. A high DF value indicates not only a more focalized source distribution, but also that the inverse method localized the estimated source to the correct location. A small DF value indicates either a blurred solution (if the LE/CME value is low) or mislocalized source reconstruction and/or spurious sources (if the LE/CME value is high).

These validation metrics were used to compare the different models and constraints to the original model at varying noise levels and with varying source spatial extents.

## 5.2 Head Model Setup for Lead Field Matrix Analysis

### 5.2.1 Electrode Positioning

Two additional electrode sets were generated by repositioning the  $z_c$  center coordinate at varying levels from the original location. Model  $Z_{c-}$  and Model  $Z_{c+}$  shift the center coordinate below ( $Z_{c-}$ ) and above ( $Z_{c+}$ ) the initial center, respectively, with an average displacement of 4.5mm and range of 0-7mm. The displacements of each electrode from the Base Model are shown in Table 2 and Figure 10. The electrode shifts were measured as the Euclidean distance between the original electrode positions and the new positions. The source localization accuracy for these shifted electrode locations was compared to the head model with the original electrode positioning (Base Model).

**Table 2 Displacement of electrodes.** Electrode locations move as the center shifts below ( $Z_{c-}$ ) and above ( $Z_{c+}$ ) the initial center of the head model. The Euclidean distance between the original and new electrode locations are displayed below.

No.	Label	$Z_{c-}$ (mm)	$Z_{c+}$ (mm)	No.	Label	$Z_{c-}$ (mm)	$Z_{c+}$ (mm)
1	Fp1	4.1	6.0	17	T5	3.7	7.1
2	Fp2	4.1	6.0	18	T6	5.7	6.0
3	F3	3.7	4.5	19	FZ	5.1	3.6
4	F4	5.7	4.5	20	CZ	0.0	0.0
5	C3	3.7	3.0	21	PZ	1.4	4.2
6	C4	3.5	3.0	22	Fpz	4.1	6.1
7	---	5.8	4.0	23	---	3.7	1.0
8	---	3.6	5.0	24	---	3.7	1.4
9	P3	2.4	4.5	25	---	5.2	6.7
10	P4	4.1	5.4	26	---	6.7	5.4
11	O1	4.1	6.1	27	---	4.4	4.2
12	O2	5.4	6.1	28	---	5.7	5.0
13	F7	4.9	6.1	29	F37	6.2	5.0
14	F8	5.1	6.0	30	F48	5.4	6.1
15	T3	5.1	6.0	31	FC3	4.6	2.0
16	T4	4.2	6.0	32	FC4	4.1	2.2

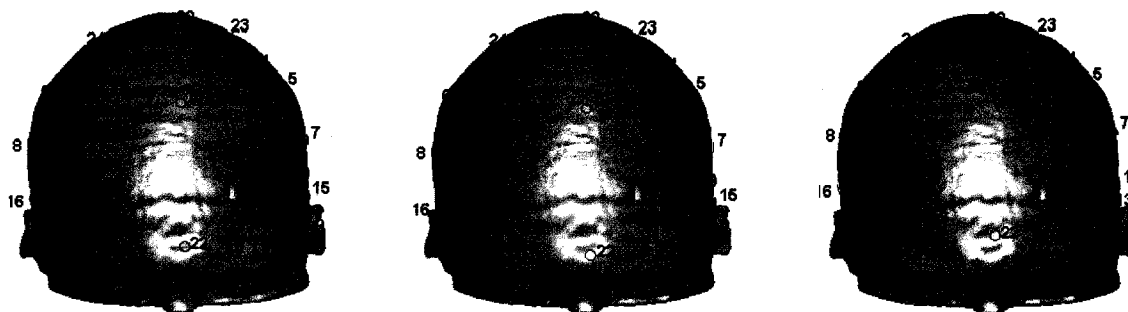


**Figure 10 Electrodes shift as center position of head model shifts.** (A) illustrates electrode positions for the estimated center coordinate of the head (Base Model), while (B) is for the  $Z_C^-$  Model, and (C)  $Z_C^+$  Model. The red circles represent the standard 20 electrodes typically used in epilepsy research, while the blue circles are the electrodes that were added for more detailed frontal lobe analysis.

## 5.2.2 Electrode Distribution

The effect of a non-uniform electrode distribution was tested by removing the following electrodes: numbers 7-8 and 23-32. Figures 8 and 10 illustrate this 20-electrode uniform distribution in comparison with the original non-uniform 32-electrode configuration (Elec20 Model vs. Base Model). The red circles represent the 20-electrode configuration, while the blue circles designate the extra electrodes placed at the front of the scalp for the 32-electrode configuration (Base Model).

## 5.2.3 CSF-Skull Boundary Delineation

We shifted the CSF-skull boundary by increasing the thickness of the cerebrospinal fluid by 2mm. This effectively thinned the skull layer while extending the CSF tissue of the volume conductor model. The CSF layer was thickened by adding a boundary of voxels ( $1\text{mm}^3$ ) twice to the existing CSF layer. This head model is termed CSF2.

## 5.2.4 Variations in Skull-to-Brain Conductivity Ratio

Two different head models were created to test the effect of the skull-to-brain conductivity ratio on source localization accuracy. The original Base Model employed

the recently accepted ratio of 1/15, while Model 1/30 altered the conductivity ratio slightly to 1/30 to represent the possible variations in the ratio as found in recent literature (Geddes and Baker, 1967; Oostendorp et al., 2000; Gonçalves et al., 2003a; Gonçalves et al., 2003b; Lai et al., 2005). Model 1/80 decreased the skull-to-brain conductivity ratio to the formerly accepted value of 1/80 (Geddes and Baker, 1967).

### **5.2.5 White Matter Anisotropy**

We constructed three different head models to study the effect of white matter orthotropic conductivity on source localization. Model WhiteY had the same conductivity properties as the Base Model, except that white matter conductivity increased tenfold in the  $y$  direction ( $y$  coordinate from posterior to anterior,  $x$  coordinate from left to right,  $z$  coordinate from superior to inferior). The conductivity of white matter increased in the  $x$  direction for the WhiteX Model and in the  $z$  direction for the WhiteZ Model.

## **5.3 Inverse Problem Setup for *a priori* Constraints**

Two different constraints were introduced to the inverse problem: normal source orientation and SPECT information.

### **5.3.1 Normal Dipolar Orientation**

Source localization results from the Base Model with no fixed dipolar orientation were compared to the same head model with the sources constrained to normal orientation (Normal Model). The orientation of the dipoles was fixed to be perpendicular to the inner cortical surface along the solution space, pointing towards the outside of the brain. This orientation was determined by finding the three dimensional gradient of the smoothed surface along the dipolar solution space. The gradient vector field was oriented

at each dipolar source along the largest variation of the smoothed cortex along the solution space. The surface was smoothed by a linear Savitzky-Golay filter. The normal orientation vector was normalized to a length of one in order to ensure equal magnitude for all dipole locations. In order to compare the source localization results from the normal orientation constraint to no orientation constraint, the absolute value of the estimated current density for the normal orientation constraint was calculated.

### 5.3.2 SPECT Information

The functional SPECT constraint was added to the inverse problem with the normal orientation constraint (Section 2.3.3.1). The size of the SPECT activity was set to an area of  $3\text{cm}^2$  instead of the typically tested  $1\text{mm}^2$  area in order to represent the relatively lower spatial resolution of SPECT as well as to represent a realistic area of activation found on SISCOM images. To quantitatively evaluate the effects of varying SPECT weighting levels, we set up the following cases: (1) no *a priori* SPECT constraint (Normal Model); (2) SPECT constraint centered on the midpoint of the original source (accurate *a priori* information); and (3) SPECT constraint placed at increasing distances from the original source location (inaccurate *a priori* information). For both the accurate and inaccurate cases, the diagonal components of the weighting matrix  $W_f$  were set to a value of 1.0 at the source locations with SPECT activity. The diagonal components of  $W_f$  corresponding to no SPECT activity were set to three different weights: 1.5 (light SPECT weighting), 2.5 (medium weighting) or 10 (strong weighting). If the diagonal components without SPECT signal were set to a value of one, this would correspond to no SPECT weighting (case 1).

For quantitative tests and the inaccurate *a priori* case, the distance between the center of the SPECT activity and the center of the original source location was divided into the following ranges: 1-20, 20-40, 40-60, and >60 mm. The specific location of the center of SPECT activity was randomly selected from these four ranges. The inverse problem was solved for each of these forward simulations. Noise was added to the simulated EEG signal at SNR levels of Infinity, 20, 10, and 5 dB.

For qualitative analysis, in order to test the effects of *a priori* SPECT information on clinical EEG data, the area of SPECT activity was set to the right frontal lobe, as shown in Figure 11. Three different SPECT weightings were tested and compared for this same activated region: 1.5 (light SPECT weighting), 2.5 (medium weighting) or 10 (strong weighting).



**Figure 11 Qualitative setup for SPECT analysis.**  
The highlighted region shows the assigned area of SPECT activity used for qualitative analysis

## 5.4 RESULTS

The effects of head model precision and *a priori* information were evaluated by comparing the different source localization results to the same head model termed Base Model. The inverse problem was solved for 2500 trials of randomly placed dipoles with strengths of  $5\text{nA}\cdot\text{m}^2$ , and with varying spatial extents of  $1\text{mm}^2$ ,  $1\text{cm}^2$ , and  $6\text{cm}^2$ . The mean values of the validation metrics for the Base Model are presented in Table 3 with the standard error of mean values in parentheses. Since most validation metric values are very similar for spatial extents of  $1\text{mm}^2$  and  $10\text{mm}^2$ , these findings are typically presented as combined results.

The average localization error (LE) for neural sources with a spatial area of  $60\text{mm}^2$  was slightly higher than for smaller dipolar sources (SNR=Inf, LE = 24 vs. 20 mm). On the other hand, the center of mass error (CME) for the varying spatial extents were very similar (SNR=Inf, CME = 12 vs. 13mm), which implies that localization accuracy was comparable across the varying neural source sizes. The slightly higher deviation in localization error for the larger dipolar sources may be a result of the localization error distance metric considering only the *maximum* position of the reconstructed activity instead of its center of mass. With a larger original dipolar source, the maximum value of the reconstructed current density may deviate from the original source location, while the center of mass remains unaffected by the source size, as indicated by the center of mass error. Our results indicate that the typically used LE metric is not as sensitive of a technique for comparing localization accuracy across different source sizes in comparison to the CME metric. Therefore, in order to compare

localization results across different-sized dipolar sources, we used the CME metric in this study.

For low noise levels (SNR  $\geq$  20dB), the average center of mass error for the estimated source current density with the Base Model was less than 2cm. However, for higher noise levels (SNR  $\leq$  10dB), the average center of mass error was considerably higher ( $\geq$ 4cm), especially considering that the length of the patient's scalp was only approximately 15cm. Such large CME indicates that the LORETA-like inverse method was unable to regularize noisier EEG signals.

For all noise levels, the degree of focalization (DF) of the source current density varied dramatically as the size of the dipolar source changed. The small DF for both 1mm<sup>2</sup> and 10mm<sup>2</sup> sources demonstrate the inability of the inverse problem to yield focused current density within the original spatial distribution of the source (SNR=Inf, DF = 3.9E-04 and 4.6E-02, respectively). This is expected with LORETA-like solutions, since the smoothness constraint of this inverse method typically leads to blurred current density. The inverse problem was only capable of localizing the majority of the energy for the larger 60mm<sup>2</sup> sized sources, as indicated by the higher degree of focalization values (SNR=Inf, DF = 0.77). For all source sizes, as the noise in the EEG signal increased, the DF decreased. With correspondingly high center of mass error, this indicates that the magnitude of the current density reduced within the correct region of the cortical sheet, and spurious sources were reconstructed within the SCD.

Figures 12 and 13 illustrate the qualitative source localization results from the clinical EEG data for the Base Model. The SCD distribution is shown for time-slices 185 and 390 from the EEG, with both time-slices corresponding to moments of activation of

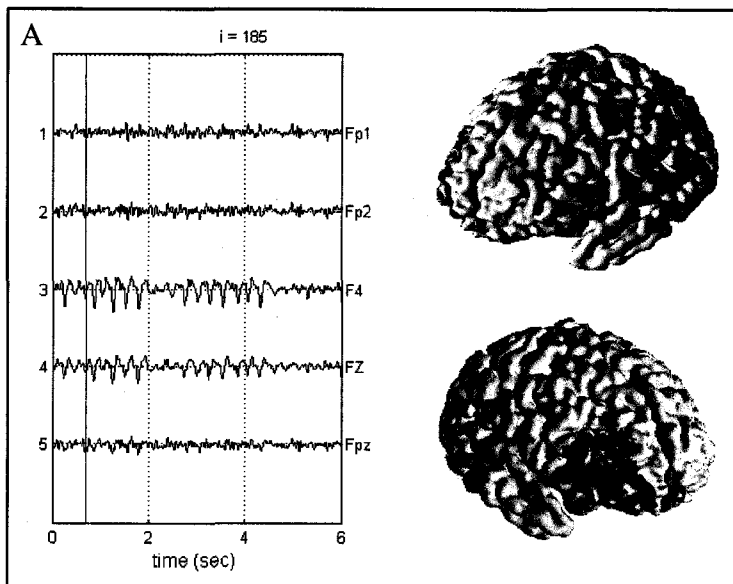


the neural sources from epileptic activity. For time-slice 185, the Base Model reconstructed source current distribution concentrated on the right frontal lobe. Time-slice 390 had more overall activity, with a hotspot at the right side of the frontal lobe as well as the mid-frontal section of the cortex. Although the concentrated activity for slice 390 extended further along the right lobe, there was also activity along the left lobe of the cortex. Time-slice 390 also illustrated very mild activity at the top of the cortical surface.

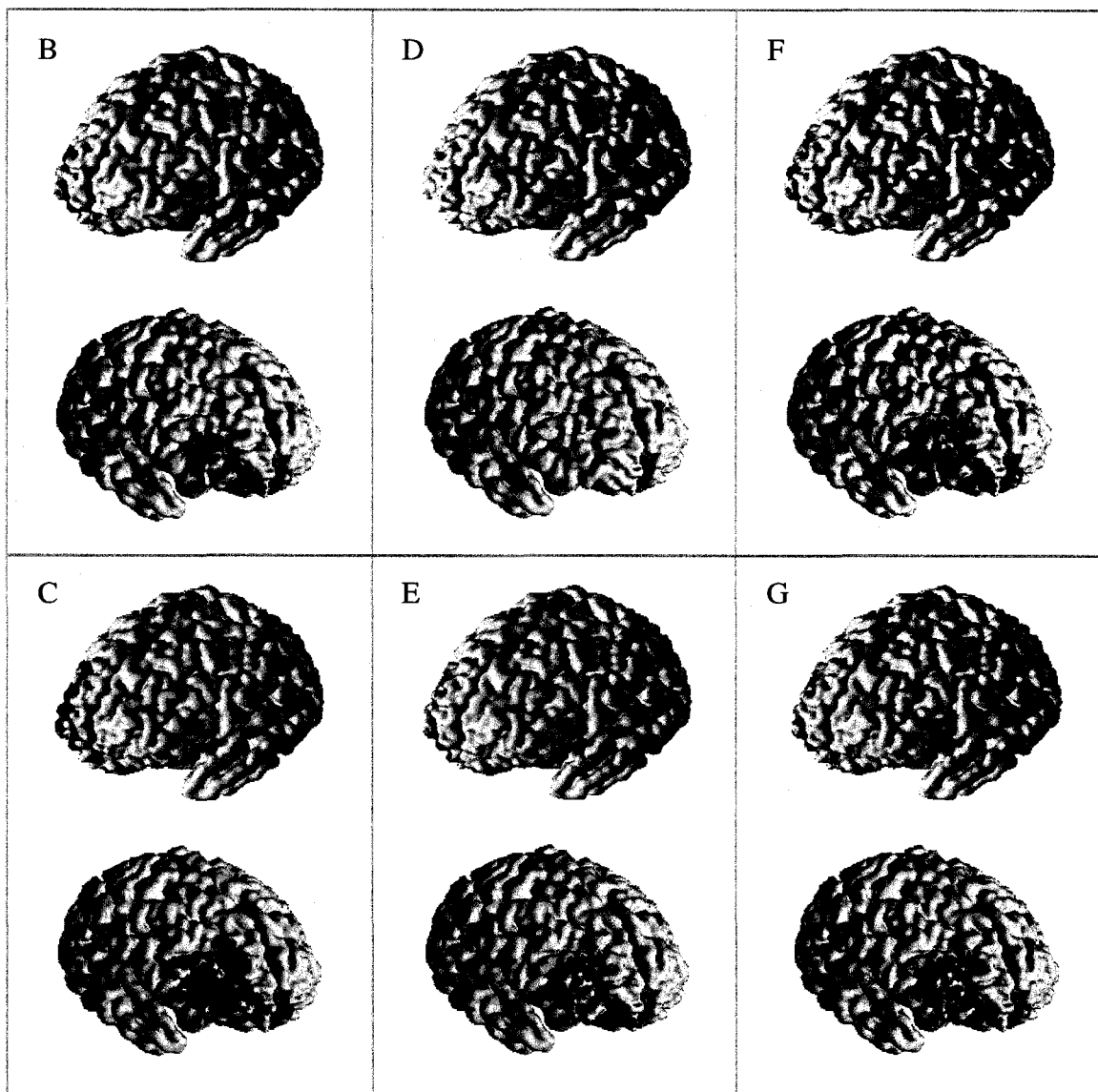
The results for the Base Model of both the validation metrics and the clinical EEG data were compared and contrasted to the source localization results from varying volume conductor models and *a priori* constraints, as described in Sections 3.1 and 3.2. The source current densities obtained from clinical EEG were normalized to the same maximum and minimum values across the different head models such that the activity could be compared.

**Table 3 Mean values and (standard error of mean) for the Base Model.** The Localization Error (LE), Center of Mass Error (CME), and Degree of Focalization (DF) validation metrics are shown for varying source spatial extents (1, 10, and 60mm<sup>2</sup>) and varying noise levels (Inf, 20, 10, and 5dB).

Validation Metric	Spatial Extent	SNR			
		INF	20 dB	10 dB	5 dB
LE (mm)	1-10mm <sup>2</sup>	19.6 (0.2)	22.0 (0.3)	49.4 (0.9)	67.7 (0.9)
	60mm <sup>2</sup>	23.5 (0.2)	26.3 (0.5)	58.1 (0.9)	70.0 (0.8)
CME (mm)	1-10mm <sup>2</sup>	13.4 (0.1)	14.0 (0.2)	34.9 (0.6)	54.3 (0.7)
	60mm <sup>2</sup>	12.3 (0.2)	13.9 (0.3)	39.7 (0.8)	55.9 (0.9)
DF	1mm <sup>2</sup>	3.9E-04 (1.3E-05)	3.8E-04 (1.3E-05)	3.0E-04 (9.9E-06)	2.1E-04 (6.9 E-06)
	10mm <sup>2</sup>	4.6E-02 (1.1E-03)	4.5E-02 (1.1E-03)	3.6E-02 (1.1E-03)	2.5E-02 (0.9E-03)
	60mm <sup>2</sup>	0.77 (0.8E-02)	0.75 (0.9E-02)	0.65 (1.0E-02)	0.45 (0.9E-02)



**Figure 12 Source current density of time slice 185 for head model variations.** The source current density is shown for the clinical EEG data of (A) Base Model, (B)  $Z_c^-$  Model with center coordinate shifted below the initial center, (C)  $Z_c^+$  Model with center shifted above the initial center, (D) Elec20 with 20-electrode configuration, (E) CSF2 with 2mm thicker CSF layer, (F) 1/30 Skull-to-Brain ratio, and (G) 1/80 Skull-to-Brain ratio.



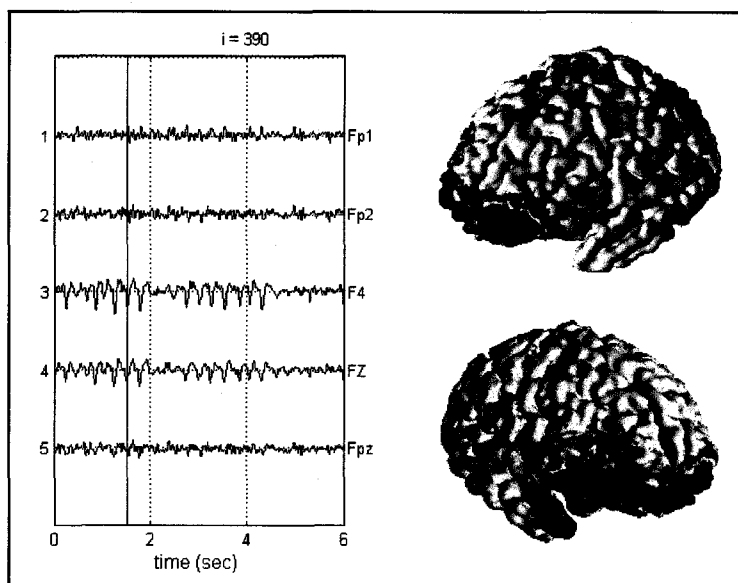
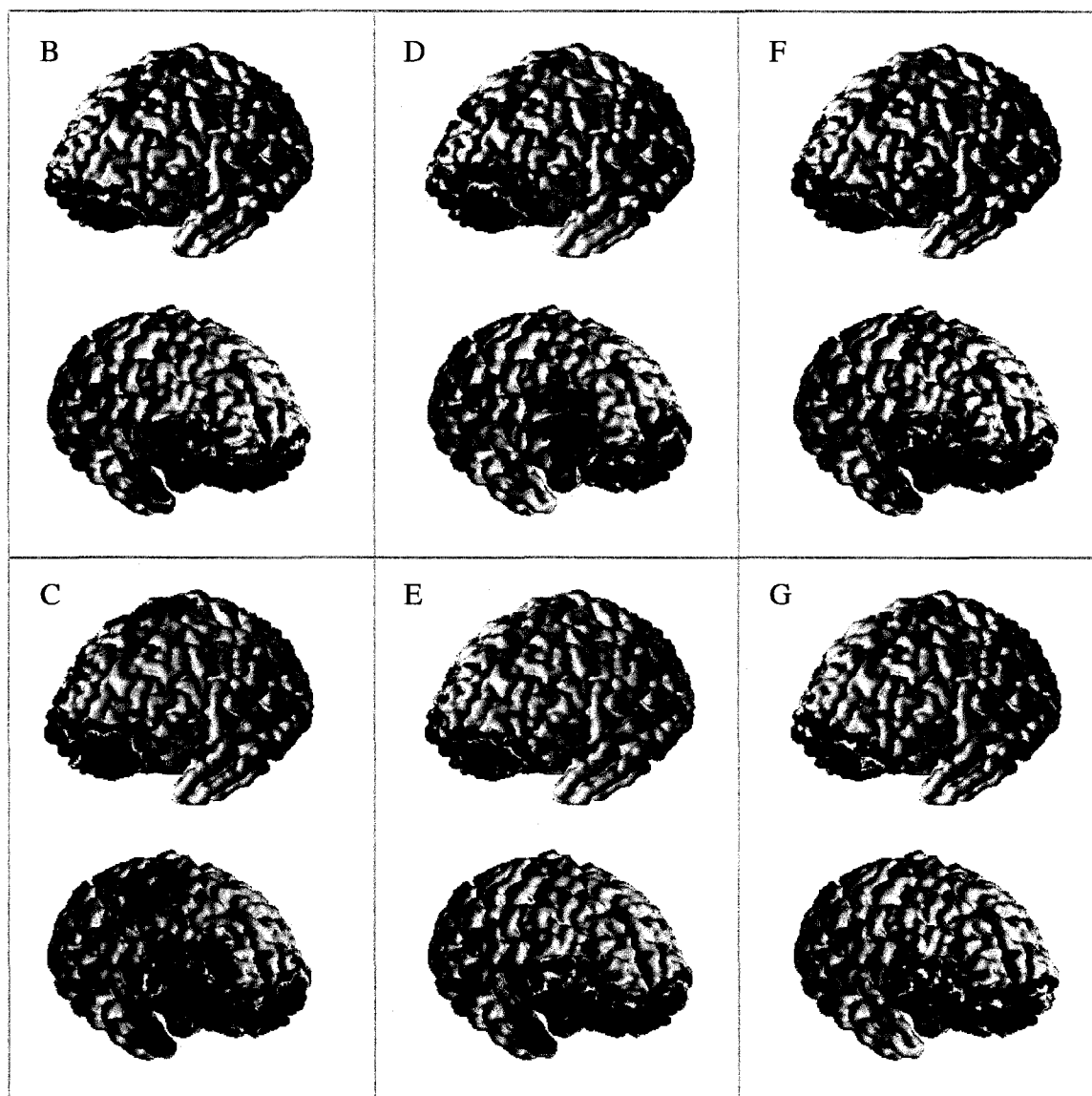


**Figure 13 Source current density of time slice 390 for head model variations.** The source current density is shown for the clinical EEG data of (A) Base Model, (B)  $Z_c^-$  Model with center coordinate shifted below the initial center, (C)  $Z_c^+$  Model with center shifted above the initial center, (D) Elec20 with 20-electrode configuration, (E) CSF2 with 2mm thicker CSF layer, (F) 1/30 Skull-to-Brain ratio, and (G) 1/80 Skull-to-Brain ratio.



## 5.4.1 Effects of Lead Field Matrix Accuracy

This section presents the effects of variations of the volume conductor model on the source localization accuracy, using standard validation metrics (CME, DF) and qualitative analysis (clinical EEG data). The validation metrics were calculated for 2500 trials of randomly placed dipoles with strengths of  $5\text{-nA}\cdot\text{m}^2$  and varying spatial extents of  $1\text{mm}^2$ ,  $10\text{mm}^2$ , and  $60\text{mm}^2$ . The potentials measured at the scalp electrodes of the Base Model from the forward problem were used as inputs to the inverse problem for the various volume conductor models. The source current density (SCD) at each source location was obtained by calculating the magnitude of the reconstructed dipolar activity.

### 5.4.1.1 Electrode Positioning

Table 4 demonstrates the mean values for validation metrics (CME and DF) of the altered electrode positions, with the center of the head model shifted above ( $Z_{c+}$ ) and below ( $Z_{c-}$ ) the original  $z_c$  position. The results for the Base Model, with the center of the head positioned at the original  $z_c$  location, are presented again in this Table for comparison. Although the degree of focalization varied significantly for the different spatial extents, the values changed consistently across the different head models for the different dipolar source sizes. Therefore, the DF values for only the  $60\text{mm}^2$  dipolar sources are shown.

The mean values for CME and DF metrics for the 2500 randomly placed dipoles did not vary by more than 3.3mm and 0.3, respectively, as the electrode positions shifted away from the Base Model. These results indicate that, in general, the accuracy of the inverse problem did not change significantly as the electrode positions moved by an average of 4.5mm and a maximum of 7mm.

The source current distribution for the clinical EEG data is shown in Figures 12 and 13; the source current density in Figures 12/13B is for the  $Z_c^-$  Model and Figures 12/13C is for the  $Z_c^+$  Model. For the  $Z_c^-$  Model and time-slice 185, the region of activation was smaller and much lower in magnitude than the Base Model. The hotspot remained in relatively the same region of the brain, although the concentrated area for the Base Model extended slightly higher on the cortical surface than the area for model  $Z_c^-$ . In time-slice 390, the mid-frontal region of the cortical surface had relatively the same activity for both the  $Z_c^-$  and the Base Model. However, the activity on the right frontal lobe extended further up the cortical sheet for the Base Model. For the  $Z_c^+$  head model and time-slice 185, the activity was again relatively the same as the Base Model, but the

**Table 4 Mean and (standard error of mean) for the Base Model and for variations in the head model.** The variations shown are with: the center of the head shifted above ( $Z_c^+$ ) and below ( $Z_c^-$ ) the original  $z_c$  position; thicker CSF tissue (CSF2); increase in white matter conductivity in the x (WhiteX), y, (WhiteY), and z (WhiteZ) direction; and normal orientation constraint (Normal).

Validation Metric	Head Model	SNR (dB)			
		INF	20	10	5
Center of Mass Error (CME, mm)	Base	13.0 (0.1)	14.0 (0.1)	36.5 (0.5)	54.8 (0.6)
	$Z_c^+$	13.7 (0.1)	15.0 (0.2)	39.8 (0.5)	56.1 (0.6)
	$Z_c^-$	13.7 (0.1)	14.5 (0.1)	38.0 (0.5)	56.7 (0.6)
	CSF2	13.6 (0.1)	14.0 (0.1)	32.6 (0.5)	51.8 (0.6)
	WhiteX	13.0 (0.1)	13.4 (0.1)	30.4 (0.4)	49.7(0.5)
	WhiteY	13.5 (0.1)	14.1 (0.1)	33.4 (0.5)	52.5 (0.6)
	WhiteZ	13.3 (0.1)	14.6 (0.1)	34.1 (0.5)	52.2 (0.6)
	Normal	13.7 (0.1)	14.7 (0.1)	36.3 (0.5)	54.0 (0.5)
Degree of Focalization (DF)	Base	0.77 (0.8E-02)	0.75 (0.9E-02)	0.65 (1.0E-02)	0.45 (0.9E-02)
	$Z_c^+$	0.77 (0.8E-02)	0.78 (1.1E-02)	0.67 (1.1E-02)	0.47 (1.1E-02)
	$Z_c^-$	0.77 (0.9E-02)	0.77 (0.9E-02)	0.67 (1.1E-02)	0.46 (0.9E-02)
	CSF2	0.77 (0.8E-02)	0.77 (0.9E-02)	0.63 (1.1E-02)	0.44 (1.0E-02)
	WhiteX	0.79 (0.8E-02)	0.77 (0.8E-02)	0.68 (1.0E-02)	0.48 (0.9E-02)
	WhiteY	0.82 (1.0E-02)	0.84 (1.0E-02)	0.75 (1.1E-02)	0.53 (1.0E-02)
	WhiteZ	0.81 (0.9E-02)	0.82 (1.0E-02)	0.65 (1.1E-02)	0.44 (0.9E-02)
	Normal	1.36 (1.5E-02)	1.39 (1.9E-02)	1.07 (1.8E-02)	0.69 (1.5E-02)

hotspot spread twice as far upwards along the cortical sheet. This was also true for time-slice 390, with the  $Z_c+$  head model leading to the most amount of activity on the cortical surface from the three different electrode position models, and with the hotspot expanding upwards along the cortical surface. There was also more current density at the top of the cortex for the  $Z_c+$  head model.

Comparing the three electrode position models, as the center of the head model shifted from  $Z_c-$  to  $Z_c$  to  $Z_c+$ , the concentrated region of SCD spread further upwards along the cortical surface. However, the hotspot region reconstructed from the  $Z_c-$  Model continued to remain active for the other two models ( $Z_c$  and  $Z_c+$ ) as the center position progressed up the head model. The hotspot of the reconstructed current density simply expanded upwards along with the movement of the electrode positions.

Although the quantitative validation metrics indicate the electrode positions did not have an effect on the estimated source current density, the qualitative results from the clinical EEG data suggest that the shift in electrode positions does have an effect on the source localization results. The electrode positioning had the greatest effect on the dipolar sources situated near the right frontal region of the cortex, with the source current distribution spreading upwards as the electrode positions shifted upwards. The electrodes located near the right frontal region of the head were numbers 4, 14, 26, and 30. These electrodes had an average displacement of 5.7mm for the  $Z_c-$  Model and 5.5mm for the  $Z_c+$  Model. These results imply that dipolar sources situated near electrode locations that shifted may be affected more by the position alterations.

### 5.4.1.2 Electrode Distribution

In order to compare quantitatively the head model with fewer overall electrodes (Elec20) to the Base Model, the validation metrics for the Elec20 Model were calculated with no noise added to the simulated EEG signal. Removing electrodes from the Base Model would modify the noise distribution in the inverse calculations. The average center of mass error with no noise for the Elec20 Model was 14.9mm, in comparison to 13mm for the Base Model. The mean degree of focalization for the  $60\text{mm}^2$  dipolar sources and the Elec20 Model was 0.6, while the mean degree of focalization for the Base Model was 0.77. The degree of focalization also reduced for the smaller source size ( $1\text{mm}^2$ :  $2.6\text{e-}2$  (Elec20) vs.  $4.6\text{e-}2$  (Base);  $10\text{mm}^2$ :  $2.4\text{e-}4$  vs.  $3.9\text{e-}4$ ). The lower degree of focalization with relatively the same center of mass error indicates that the source current density was localized to the same location, but that less energy was reconstructed within the original source location. This may imply spurious sources within the reconstructed signal or a properly estimated source current density but with reduced magnitude.

The source current density from clinical EEG data (Figures 12 and 13) gives more insight into the source localization results for the Elec20 Model. With the same threshold set as for the Base Model, no activity was illustrated at time-slice 185, while the only hotspot in time-slice 390 was in the mid-frontal region of the cortex. The inverse problem with Elec20 reconstructed activity with reduced magnitude within the right frontal area of the cortical surface for time-slice 390, spreading twice as far upwards along the cortical sheet. Further, the source current density in the mid-frontal region of the cortex was more focused along the right side of the fissure, while the left side contained a larger area of intense current density. Thus, removing extra frontal electrodes (Elec20 Model) led to

reduced reconstructed activity near these electrode locations and a change in the overall current distribution. Both quantitative and qualitative results indicate that removing the extra frontal electrodes removed valuable information about the source activity, with a major impact on the source current density distribution.

#### **5.4.1.3 CSF-Skull Boundary Delineation**

The validation metrics for the head model with an extended 2mm CSF boundary (CSF2 Model) are shown in Table 4. The mean value for all metrics was the same as for the Base Model, with the largest difference in average CME only 3.9mm and in average DF only 0.02. These results imply that adding 2mm to the width of the CSF boundary does not have a major impact on the localization accuracy of the inverse solution.

The quantitative results agree with qualitative source localization results obtained from clinical EEG data, as shown in Figures 12 and 13. The source current density distribution for Model CSF2 for both time-slices 185 and 390 was nearly identical to the Base Model, with a slight reduction in intensity of signal. The 2mm thicker CSF boundary produced more focused current density than the Base Model, but the difference between the two different source distributions was almost indistinguishable in time-slice 390. For a smaller signal such as in time-slice 185, thickening the CSF tissue had a greater impact on the intensity of the reconstructed source current density.

#### **5.4.1.4 Skull-to-Brain Conductivity Ratio**

Figure 14 displays the mean CME and DF for the three different head models with skull-to-brain conductivity ratios of 1/15 (Base Model), 1/30, and 1/80 for 2500 random trials. Although the DF metric varied significantly for the different spatial extents, we only present the results for the 60mm<sup>2</sup> sources since changes in the DF metric



were consistent across the different source sizes. The mean value of the validation metrics are displayed for signal to noise ratios of: INF (No Noise), 20 dB, 10 dB, and 5 dB.

For minimal noise levels (SNR  $\geq$  20 dB), the center of mass error was smallest for the Base Model with a conductivity ratio of 1/15. The mean center of mass error increased slightly as the skull to brain ratio decreased to 1/80, but only by approximately 5mm. The difference between validation metrics for the 1/30 skull-to-brain conductivity ratio in comparison to the Base Model were minimal, especially as the noise levels increased. On the other hand, the validation metrics for the 1/80 model shifted significantly from the Base Model as the EEG noise levels increased. The mean center of mass error for the head model with 1/80 conductivity ratio was moderately lower than the other head models for higher noise levels, with a reduction in mean CME from the Base Model of 5.1mm for SNR = 10dB and of 8.4mm for SNR = 5dB. At the same time, the DF values for the 1/15 and 1/30 skull-to-brain ratios decreased considerably more than the 1/80 ratio as the noise levels increased. The relatively lower center of mass error and higher degree of focalization indicates that the head model with the 1/80 conductivity ratio was less sensitive to noisy signals, with more activity reconstructed to the correct location in the cortex and fewer spurious sources for noisier signals.

Figures 12 and 13 show the source localization results for clinical EEG data for several time-slices. The alteration in the skull-to-brain conductivity ratio from 1/15 to 1/80 modified the source current distribution. Specifically, the source current density for the Base Model (1/15) spread further than the 1/80 head model, as illustrated in both time-slices 185 and 390. The overall area of activation remained relatively the same in

slice 185 for the two different head models, but the 1/80 model had much more focused current density. The discrepancy between the models was more obvious with time-slice 390. The overall source current density was much more focused for the 1/80 model, with the concentration of the current density focusing towards the fissure of the cortex. The intensity of the source current density on the right-frontal area of the lobe was approximately half as intense as the mid-frontal region for the 1/80 model, while the SCD intensity between the two cortical regions was more comparable for the Base Model. There was no activity at the top of the head for the 1/80 head model, while there was small amounts of activity for the 1/15 (Base) Model. For a skull-to-brain conductivity ratio of 1/30, the reconstructed activity was almost identical to the results from the Base Model. For slice 185, the SCD was slightly more focused, but with the center of mass in the same location; this was also true for time-slice 390.

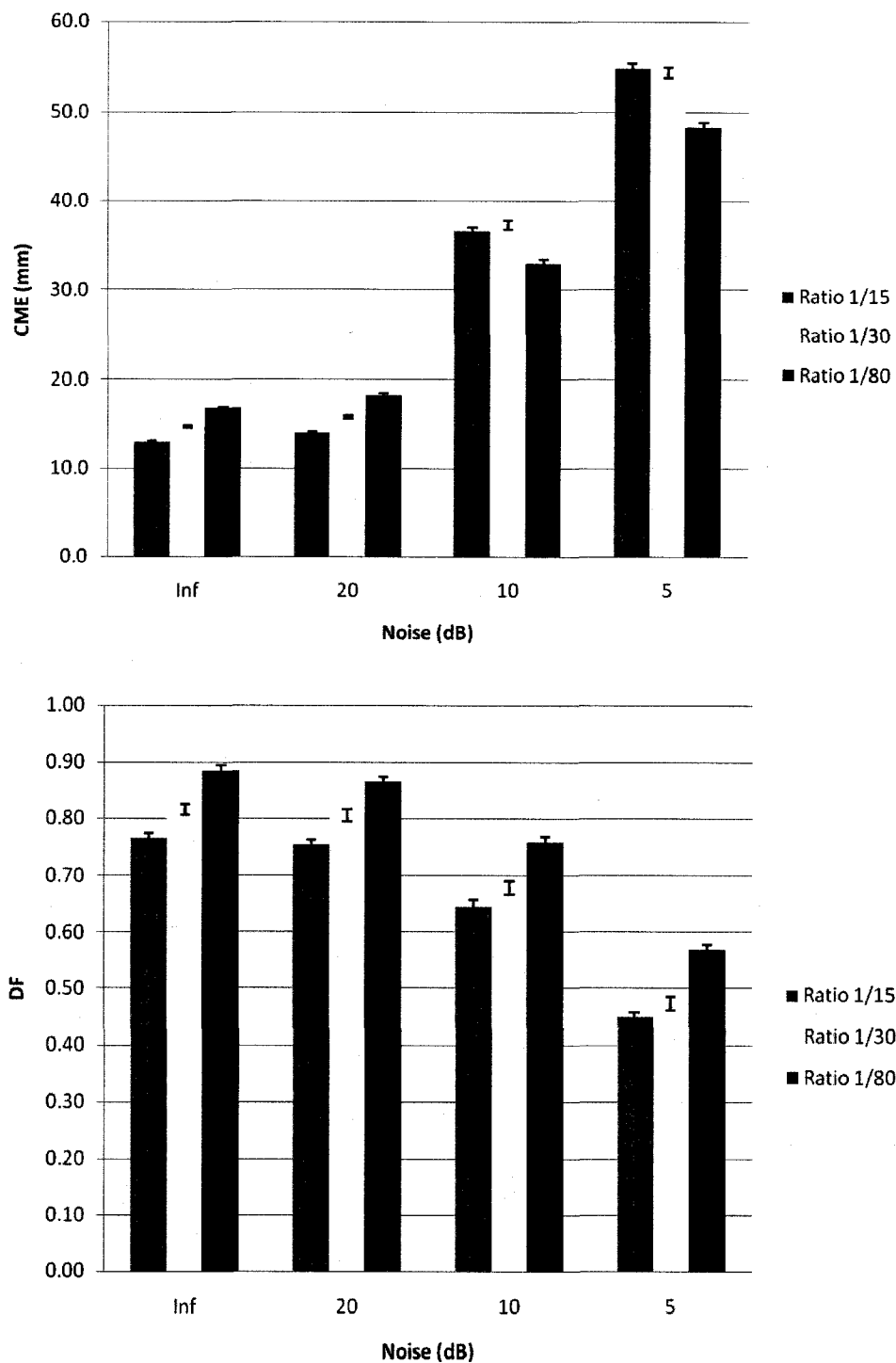
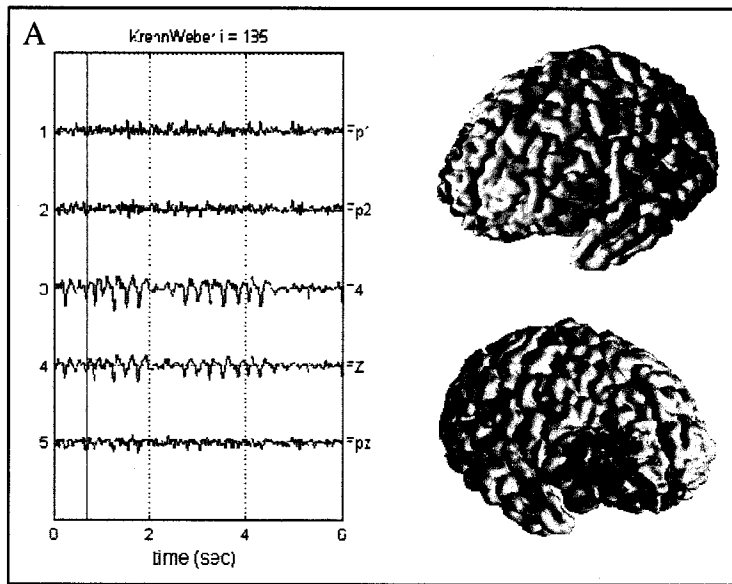


**Figure 14 Validation metrics for variations in the skull-to-brain conductivity ratios.** Mean Center of Mass Error (above) and Degree of Focalization (below) for head models with skull-to-brain ratios of 1/15 (Base Model), 1/30, and 1/80. The Center of Mass Error was highest for the 1/80 ratio for low noise levels, but lowest for high noise levels. The Degree of Focalization was highest for all noise levels for the head model with 1/80 skull-to-brain conductivity ratio.

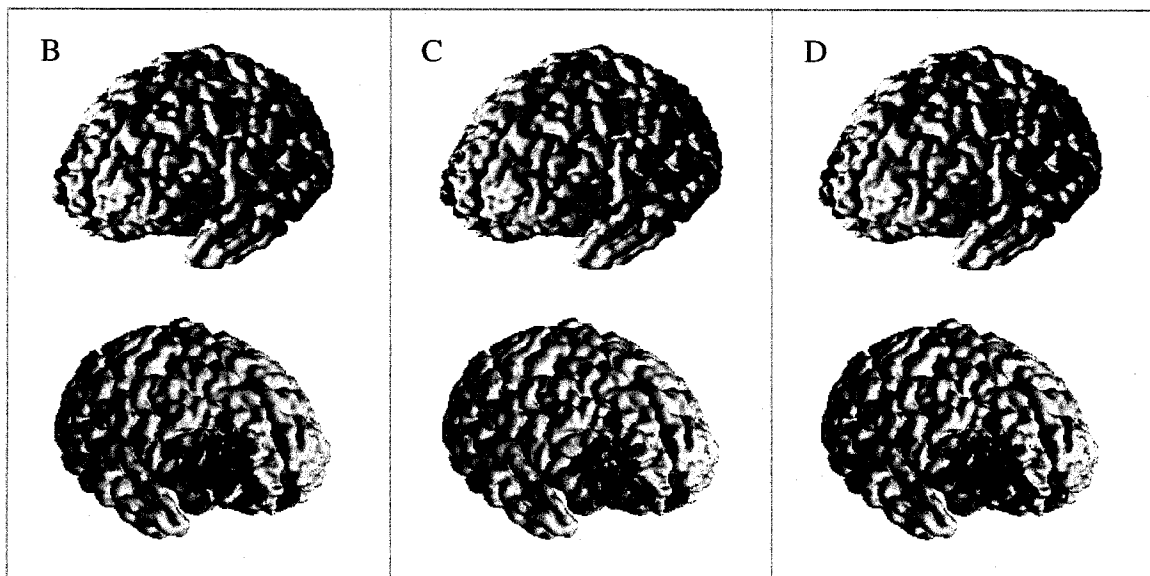
### 5.4.1.5 White Matter Anisotropy

The mean values for the validation metrics of models WhiteX, WhiteY, and WhiteZ are listed in Table 4. The average CME values for SNR  $\geq$  20dB were relatively the same across the various volume conductor models, with the largest difference in average CME from the base model only 0.6mm. For SNR  $\leq$  10dB, the CME was the same for the Base, WhiteY, and WhiteZ Models, with the largest change in error only 2.6mm. The WhiteX Model's average CME shifted somewhat more from the Base Model, with a maximum change of 6.1mm. On the other hand, the mean DF for the WhiteX volume conductor remained more or less unchanged from the Base Model, while WhiteY and WhiteZ changed by a maximum amount of 0.1 and 0.07, respectively.

The reconstructed SCD for the clinical EEG data of the three different white matter orthotropic conductivity models are illustrated in Figures 15 and 16. The SCD for the WhiteX Model was almost identical to the Base Model, as demonstrated in time-slice 185 and especially in slice 390. The current density was slightly stronger for the WhiteX Model for time-slice 185, with a small shift in location of the strongest region of the source current density. The WhiteY Model yielded a more focused current density at time-slice 185 with the concentrated region of activity approximately half in size. There was also a change in SCD distribution illustrated at time-slice 390, with the activity in the right-frontal region splitting somewhat from the mid-frontal region of the cortex. The magnitude of the current density in the right frontal region of the cortex was also reduced in comparison to the Base Model. Source localization with the WhiteZ Model led to slightly more intense SCD for both time-slices, but the activity was contained within the same region of the cortical surface.



**Figure 15 Source current density of time slice 185 for white matter orthotropic conductivity.** SCD of the (A) Base Model, and the (B) WhiteX, (C) WhiteY, and (D) WhiteZ Models, with increased white matter conductivity in the x, y, and z direction, respectively.



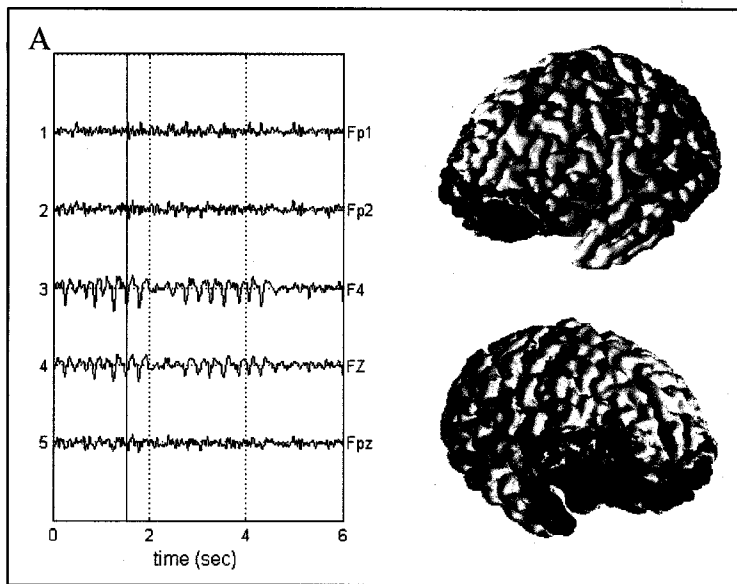
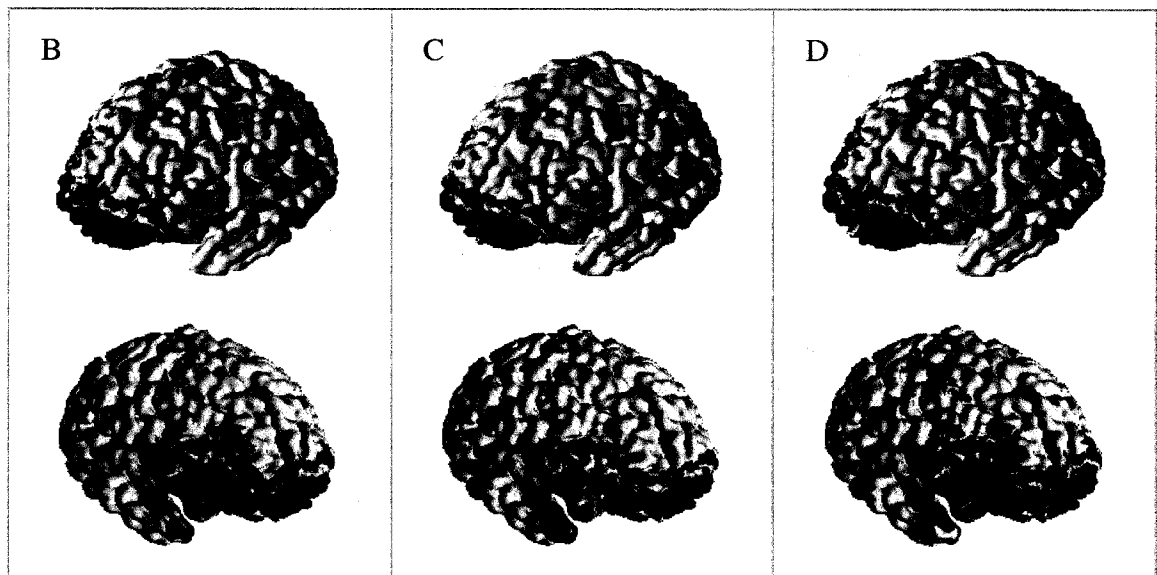


**Figure 16 Source current density of time slice 390 for white matter orthotropic conductivity. SCD of (A) Base Model, and the (B) WhiteX, (C) WhiteY, and (D) WhiteZ Models, with increased white matter conductivity in the x, y, and z direction, respectively.**



These results indicate that the SCD distribution altered to some extent with changing white matter orthotropic conductivity properties, especially the magnitude of the reconstructed current. The quantitative results also point towards a change in SCD distribution as the white matter conductivity increased in the x, y, and z directions, with small alterations in the CME or DF depending on the direction of increased conductivity. Both results imply that dipolar sources are affected differently by each directional change in conductivity, depending on the position of the source within the cortex (i.e. – dipoles along the side of the cortex may be affected differently than those at the front and back of the cortex).

## **5.4.2 Effects of *a priori* Constraints**

### **5.4.2.1 Normal Orientation Constraint**

Table 4 compares the validation metrics for the normal orientation constraint (Normal Model) to no orientation constraint (Base Model). The mean DF values are shown only for the  $6\text{cm}^2$  dipolar sources since the values varied comparably across the different source sizes for the two head models.

The mean CME was consistent for both models, even with varying noise levels. In comparison, the average DF increased significantly for the normal orientation constraint, over all source sizes and noise levels. For the larger  $60\text{mm}^2$  sources, the inverse results of the Normal Model focused the majority of the energy to the original area of the dipolar source. Although the normal orientation constraint led to a more focused source reconstruction, the center of the current density was the same as for the Base Model, as indicated by the same CME values. Thus, although the spatial resolution was improved

upon with the normal constraint, this *a priori* information did not affect the center of mass of the reconstructed source distribution.

Figures 17B and 18B show the SCD for the normal orientation inverse results for clinical EEG data, in comparison to the Base Model (Figures 17A and 18A). Both time-slice 185 and 390 illustrated much more focalized SCD in comparison to the inverse problem with no orientation constraint (Base Model), with the size of the intense region of current density reduced by half for slice 185 and by approximately a third for slice 390. However, for both time-slices the center of mass remained in relatively the same position of the cortical surface. These results agree with the quantitative analysis of the Normal Model.

#### **5.4.2.2 SPECT Information Constraint**

Figures 19 and 20 demonstrates the average CME and DF for the three different cases of the SPECT constraint and for varying levels of SPECT weighting. The three cases for the SPECT constraint shown are: (1) no *a priori* SPECT information (Normal Model); (2) SPECT information centered on the midpoint of the neural source location (accurate *a priori* information); and (3) SPECT constraint placed at increasing distances from the center of the original source (inaccurate *a priori* information). The validation metrics were compared for different weighting levels of the SPECT constraint: 1.5 (light weighting), 2.5 (medium weighting), or 10 (strong weighting). The results from case (1) correspond to the results obtained in Section 3.2.1. For the inaccurate *a priori* information (case 3), the distance between the center of SPECT activity and the center of neural source spatial extent was divided into the following ranges: 1-20, 20-40, 40-60, and >60 mm. All results correspond to a SPECT activity size of  $3\text{cm}^2$ . The DF values



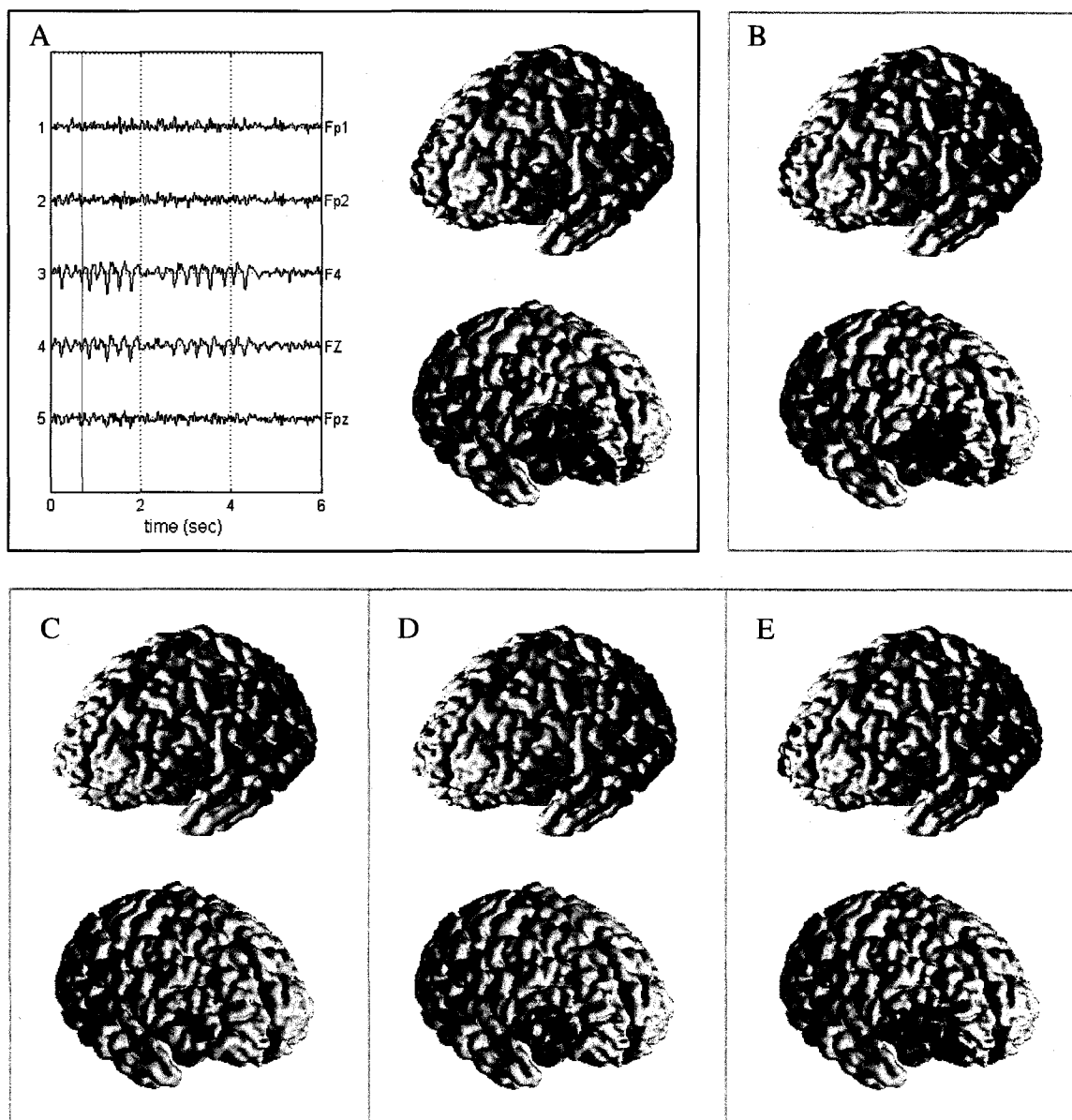


**Figure 17 Source current density of time slice 185 for *a priori* constraints.** The reconstructed source current density of the clinical EEG data is shown for the Base Model (A) vs. the Normal Model (B), with the orientation of the dipoles restricted to be normal to the cortical surface. The current density from the Normal Model was compared to the inverse results from the “strong” (C), “medium” (D), and “light” SPECT weighting.

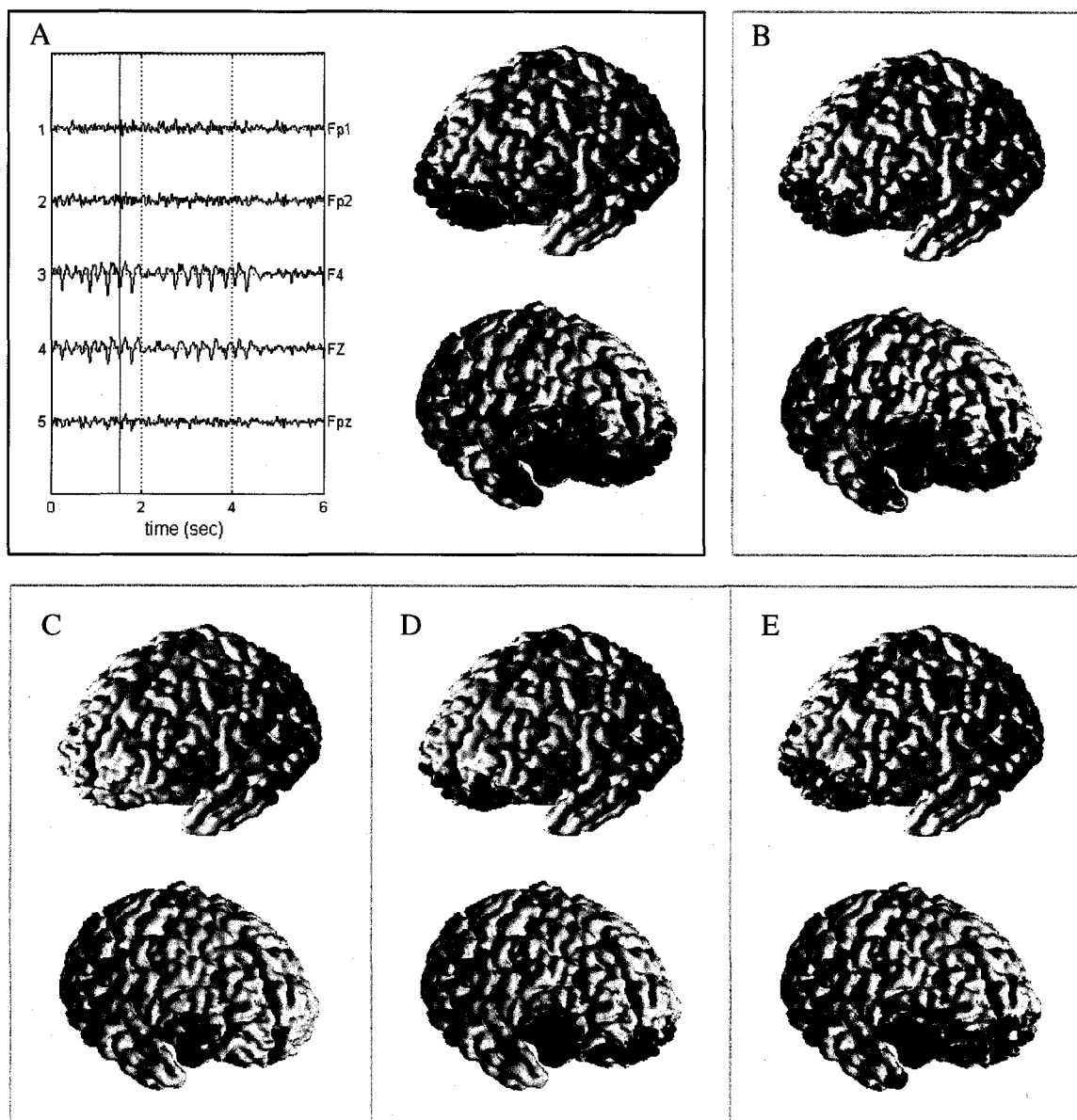


**Figure 18 Source current density of time slice 390 for *a priori* constraints.** Reconstructed source current density for time slice 390 of the clinical EEG data for the Base Model (A) vs. the Normal Model (B), with the orientation of the dipoles restricted to be normal to the cortical surface. The current density from the Normal Model (B) was compared to the inverse results from the “strong” (C), “medium” (D), and “light” SPECT weighting.

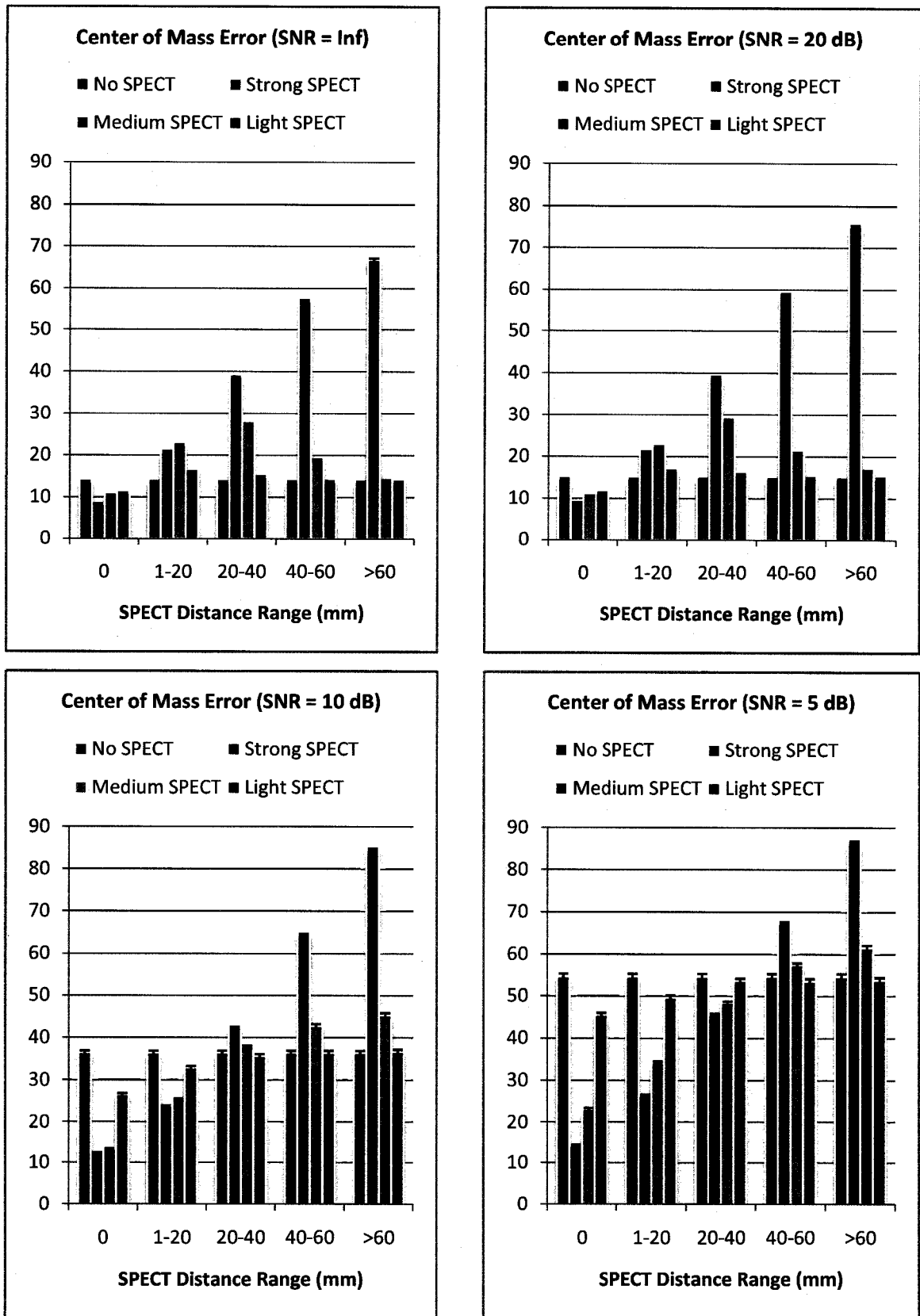
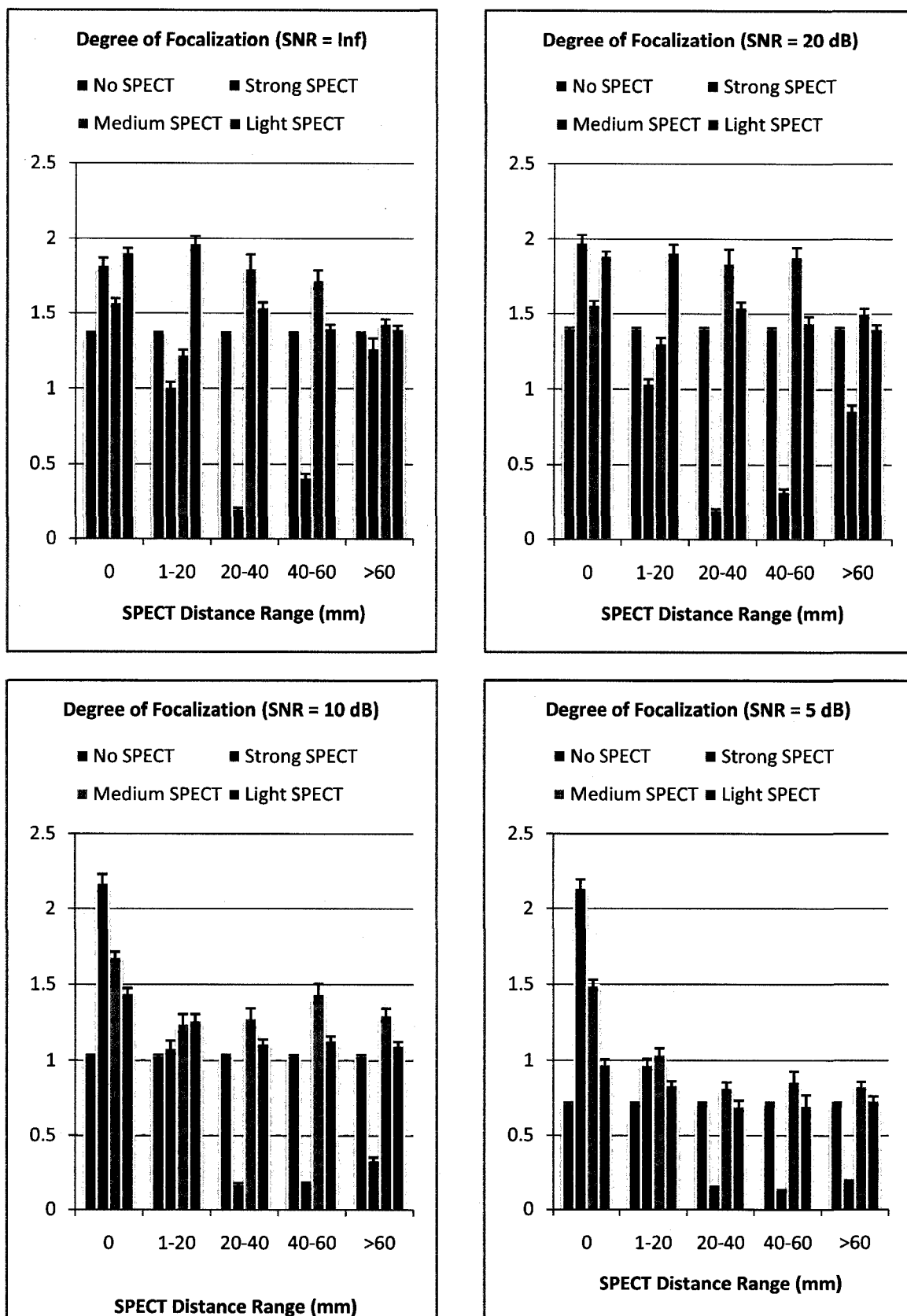


Figure 19 Center of mass error for different weighting levels of SPECT. CME is shown for SNR: INF, 20, 10, and 5dB and for distances between SPECT and source activity of: 0, 1-20, 20-40, 40-60, >60mm



**Figure 20 Degree of Focalization for different weighting levels of SPECT.** DF is shown for SNR: INF, 20, 10, and 5dB and distances between SPECT and source activity of: 0, 1-20, 20-40, 40-60, and >60mm

varied significantly for the different sizes of the original sources, but the overall pattern of change was the same. Therefore, only the results for the  $60\text{mm}^2$  sources are shown.

For a “strong” SPECT constraint with a weighting of 10, the center of mass error was much lower for accurate *a priori* information (case 2) than for no SPECT information (case 1), over all levels of noise. For example, for  $\text{SNR} = 20\text{dB}$ , the average center of mass error for case (1) was 15.2mm while for case (2) it was 9mm. However, as the distance between the SPECT activity and the neural source location increased (case 3), the mean center of mass error increased correspondingly. With no noise in the signal, even small distances ( $\leq 2\text{cm}$ ) between the SPECT information and dipolar source activity led to center of mass error that was higher than with no SPECT constraint. For example, for  $\text{SNR} = \text{INF}$  and distances of 4 to 6cm, the average CME was 5.7cm with the inaccurate SPECT constraint, while the mean CME was only 1.3cm with no SPECT constraint. The rise in center of mass error for increasing distances signifies that the SPECT information holds too much weight in comparison to the source information from the EEG signal.

The degree of focalization results for the noise-free EEG signal agree with this finding. The degree of focalization dropped dramatically as the distance increased between the SPECT and dipolar activity, up until a 6cm separation, indicating that the reconstructed source was not localized to the correct location. The DF increased slightly for distances greater than 6cm; with correspondingly high CME; this denotes that current density was present in the correct location, but there were also spurious sources.

As the noise of the EEG signal increased, the center of mass error increased slightly for both cases (2) and (3). This suggests that the source localization results were

still dependent on noise, as well as on SPECT information. The average center of mass error was still lower for accurate *a priori* information for all noise levels, and for distances  $< 2\text{cm}$  for  $\text{SNR} = 10\text{dB}$  and distances  $< 4\text{cm}$  for  $\text{SNR} = 5\text{dB}$ . However, the average center of mass error was smaller for these distance ranges from case (3) in comparison to case (1) only because the strong SPECT constraint shifted the reconstructed source activity to a distance smaller than the CME from the noisy EEG signal alone (case 1).

For all noise levels, the degree of focalization decreased considerably for all inaccurate SPECT *a priori* information in comparison to case (1), even for large distances. The smallest average DF equals 0.12 for  $\text{SNR} = 5\text{dB}$ , in comparison to 0.70 for case (1). The only instances when the degree of focalization was higher for the SPECT weighting than for no SPECT weighting was for accurate *a priori* information and for  $\text{SNR} \leq 10\text{ dB}$  with distances  $\leq 2\text{cm}$ .

For the clinical EEG data, the only reconstructed activity for the “strong” constraint was within the region of the original SPECT activity, as shown in Figures 17 and 18. In time-slice 185, minimal activity was reconstructed within the SPECT region and no activity was reconstructed from the EEG data. For time-slice 390, the reconstructed hotspot was again only within the area of the SPECT activity, with a higher magnitude of source current density because the SPECT and EEG data aligned within this region. Both time-slices illustrated that SCD that would typically be reconstructed from the EEG information was ignored if it did not align with the SPECT information.

For a “medium” SPECT constraint with a weighting of 2.5, the average CME for the accurate SPECT information (case 2) was still smaller than for no SPECT

information (case 1), similar to the “strong” constraint. For low noise levels ( $\text{SNR} \geq 20\text{dB}$ ), as the distance between the center of SPECT and dipolar activity increased towards 4cm, the CME also increased. For distances closer to the dipolar activity (1mm-2cm), the degree of focalization decreased while the center of mass error increased; this suggests that the SPECT information was influencing the final source localization result. For distances slightly further away from the dipolar source (2-4cm) and for low noise levels, the DF increased while the CME still also increased. This indicates that although the hottest spot was affected by the increasingly distant SPECT activity, there was still reconstructed activity both at the neural source and at the SPECT activity.

The increase in error as the distance increased was not as substantial as with the “strong” SPECT constraint, with the largest rise in mean CME for  $\text{SNR}=\text{INF}$  reaching a value of 28mm for a distance range of 2-4cm. These results indicate that for low noise levels ( $\text{SNR} \geq 20\text{ dB}$ ), the SPECT constraint still influenced the source localization results for distances up to 4cm between the center of the SPECT and dipolar activity. For the distance range 4-6cm, the CME decreased again to 19mm (in comparison to the Normal Model value of 14mm) while the mean DF remained relatively high with an average of 1.73 (Normal Model = 1.36). The center of mass error decreased slightly more for distances greater than 6cm. Therefore, for large distances and low noise levels, the SPECT constraint has limited influences on the reconstructed source activity.

For  $\text{SNR} \leq 10\text{dB}$ , the center of mass error continued to increase as the distances between the dipolar and SPECT activity increased, as a result of the noisy EEG signal. The increase in CME was not as substantial as for the “strong” SPECT constraint. Although the degree of focalization decreased slightly as the noise levels increased, the

mean values for case (2) and (3) remained higher than for case (1). Therefore, although the CME still increased with increasing noise levels, more of the energy of the reconstructed source current density was localized to the correct area of the dipolar source, no matter what the SPECT information, in comparison to the Normal Model.

The reconstructed activity from clinical EEG data for the “medium” SPECT constraint was still concentrated within the SPECT activity area, but the EEG data had a stronger influence on the source current density. For example, in slice 185, although the majority of the activity remained within the SPECT region of activation, the hotspot was localized within very close proximity to the original location from case (1). In time-slice 390, the region where the SPECT and EEG data aligned on the cortex had the strongest level of activity, while there was relatively mild activity in the region corresponding to only EEG information.

For a “light” constraint of 1.5, the CME was still smaller for accurate SPECT *a priori* information (case 2) than for no SPECT information (case 1) for all noise levels, but only by a minor amount. For example, the CME for case (2) with SNR = INF was 11mm while for case (1) it was 14mm. Unlike the “medium” and “strong” constraint results, the center of mass error increased with increasing noise even for accurate SPECT information. However, for higher noise levels, the CME for the accurate SPECT information was still lower than for no SPECT constraint. The degree of focalization remained relatively high for all noise levels and distances (cases 2 and 3), with the degree of focalization dropping off to levels comparable to no SPECT constraint (case 1) only at high noise levels (5dB). This implies that there was more source current density localized to the correct location, but there were still spurious results. Both the CME and DF results



indicate that the accurate SPECT “light” *a priori* constraint was less susceptible to noise than the inverse problem with no SPECT constraint.

The major improvement for the “light” SPECT constraint was that the center of mass of the reconstructed activity did not change substantially for inaccurate SPECT information (case 3). The only mean CME values from case (3) that were slightly higher than the error for case (1) were for distances smaller than 2cm and for SNR  $\geq$  20dB. For example, the CME for SNR = INF for a distance range of 1-20mm was 16mm while for case (1) it was 14mm. This is a reasonable result, since SPECT information within 2cm of the original dipolar source may be relevant to the overall reconstructed source activity. At the same time, the degree of focalization was higher for the SPECT-constrained inverse results than for no SPECT information, regardless of the level of noise or the amount of distance between the SPECT activity and dipolar source. The lowest average DF value for the “light” SPECT constraint was for SNR=5dB and distances of 2-4cm with a value of 0.7, which was equal to the value for case (1). These results imply that the “lightly” constrained inverse problem provided more accurate and focalized results for almost all scenarios. At the same time, the source localization results were a balance between the dipolar source activity and SPECT information, placing emphasis on the EEG information when the SPECT information did not align closely with the EEG data.

The “light” SPECT constraint provided the biggest compromise between the SPECT and EEG information, as shown with the clinical EEG analysis in Figures 17 and 18. The SCD distribution was not limited to the SPECT area of activation, as demonstrated in time-slice 185. The center of mass of the SCD shifted slightly towards the SPECT region in comparison to the Normal Model results, but the prevalent area of

current density remained slightly outside the SPECT area. Thus, the SPECT constraint affected the overall source current distribution by shifting the SCD slightly to the right, utilizing both the EEG data and SPECT information in reconstructing the source.

For slice 390, the current density was prominent at both the SPECT region of activation and the cortical area that would be reconstructed from EEG data alone. The spatial resolution was reduced for the “light” constraint in comparison to no *a priori* SPECT information. This is because the region of SPECT activation was larger than the area reconstructed from case (1). Therefore, the spatial resolution of the SCD may be limited by the spatial resolution of the SPECT data.

## Chapter 6

### Discussion

The goal of this study was to obtain the most accurate source localization results with clinically available data. Therefore, we studied the effects of head model variations, specifically those due to clinical data uncertainties, on the accuracy of the inverse problem. The effects of *a priori* information on source localization precision were also analyzed. All tests were done with a LORETA-like solution to the inverse problem and were analyzed both qualitatively with clinical EEG data and quantitatively with validation metrics calculated for randomly placed dipolar sources in the source space. The variations in both the volume conductor model, represented by the LFM, and in *a priori* information, characterized by modifications in the inverse problem, were compared to the same model termed Base Model. This model corresponded to the volume conductor head model with conventional information available from clinical data and with no additional constraints.

The source localization results from the Base Model illustrated that the LORETA-like inverse method tended to blur the estimated source current density. However, most of the energy of the source current density was reconstructed to within the spatial extent of the larger neural sources ( $6\text{cm}^2$ ). This dipolar source size corresponded to the assumed minimum source area required to observe spike and sharp waves on the scalp electrodes (Ebersole, 1997). If this assumption is correct, then the blurring from the LORETA inverse method is a reasonable result. It was also observed that the CME validation metric was a more accurate metric for comparing localization accuracy across the

different dipolar source sizes than the LE metric. Finally, the validation metrics for the Base Model suggested that the LORETA-like inverse problem was unable to regularize the EEG signal for higher noise levels, leading to spurious sources within the reconstructed source current density. The LORETA-like method was able to regularize noisy signals with  $\text{SNR} \geq 20\text{dB}$ , but produced high localization error for  $\text{SNR} \leq 10\text{dB}$ . Epileptic spikes are assumed to have noise levels between 10-20dB, so the inverse method may be able to correctly localize most of the relevant activity for epileptic patients, as demonstrated by the qualitative analysis of clinical EEG data.

## 6.1 Head Model Precision

A major concern with EEG source localization is uncertainty in electrode positions on the scalp of the volume conductor model (Khosla et al., 1999; Wang and Gotman, 2001; Michel et al., 2004). Recent studies have shown that electrode variations do not have a major effect on source localization accuracy in comparison with uncertainty due to noisy EEG signals (Khosla et al., 1999; Wang and Gotman, 2001). Our quantitative analysis agrees with these findings. For electrode position adjustments with an average displacement of approximately 4.5mm, the source localization accuracy was not affected even as the noise levels increased, as demonstrated by the validation metrics remaining relatively the same. However, as shown in our qualitative analysis, the source current distribution may vary for dipolar sources situated near the electrode locations, with the center of mass shifting slightly as the positioning changed. As the electrode positions shifted up the scalp of the head model, the source current density, especially in the right frontal region of the cortex, spread upwards as well.

Based on these findings, realistic shifts in electrode positions on the scalp have a small affect on the source distribution for dipolar sources close to these positions. However, these shifts in positions do not have an effect on the overall accuracy of the inverse problem across the entire cortical surface. This implies that the standard 10-10 electrode coordinate system can be used in approximately locating electrodes on the volume conductor model's scalp without adversely influencing the inverse solution results, as long as the area of interest is not situated near the bottom transverse plane of the coordinate system.

The results from the head model with reduced number of electrodes covering the scalp show the importance of properly covering the cortical region of interest with a denser distribution of electrodes. The quantitative results indicate that a sparser distribution of electrodes leads to a lower overall degree of focalization. This implies that the reconstructed current density becomes more diffuse as the distance between electrodes increases. This agrees with research that has shown that the source localization accuracy increases with increasing electrode density on the scalp up until 100 electrodes (Lantz et al., 2003). Further, in the clinical EEG analysis, excluding extra electrodes at the front of the head led to losing information about the overall current distribution. The concentrated activity at the right-frontal region of the cortex was not localized for either time-slice, with the only hotspot located at the mid-frontal area of the cortex. The reduction in electrodes led to a completely different source current density configuration from the model with the added frontal electrodes on the head.

Another issue with clinically available information is that the CSF-skull tissue boundary of a patient's head is difficult to segment with accessible T1-weighted MRI.

This study evaluated the effect of changes in CSF thickness resulting from segmentation errors on the inverse problem. Increasing the CSF layer by 2mm, which in turn decreased the thickness of the skull tissue layer, did not considerably change or affect the validation metrics in comparison with the Base Model. In addition, qualitative results show almost identical source current density over time for clinical EEG data. Therefore, although it may be imperative to include the CSF layer in the head model (Ramon et al., 2004 and 2006), our results indicate that slight variations in CSF segmentation do not have a major affect on source localization accuracy.

The skull-to-brain conductivity ratio is another unknown parameter in the volume conductor model. Previous inverse problem studies used a ratio of 1/80 (Geddes and Baker, 1967), but the most recent commonly accepted value is 1/15 (Oostendorp et al., 2000; Gonçalves et al., 2003 a, b; Baysal and Haueisen, 2004; Lai et al., 2005). There are still variations in literature on the conductivity ratio, with values ranging from 1/15 to 1/30 (Oostendorp et al., 2000; Gonçalves et al., 2003 a, b; Baysal and Haueisen, 2004; Lai et al., 2005). It is well known that the skull has a major impact on source localization results, due to its exceedingly low conductivity in comparison to all other cephalic tissues. The change in the skull-to-brain conductivity ratio from the previously accepted value of 1/80 to the new value of 1/15 has not been studied, to our knowledge. Therefore, we analyzed the change in source localization accuracy attributable to variations in the skull-to-brain conductivity ratio. As well as comparing the previous ratio to the most recently accepted value, we also compared the new ratio to a value of 1/30 in order to evaluate the effect of smaller variations in conductivity ratio. If small changes in skull-to-

brain conductivity ratios adversely affect the inverse results, it may be necessary to acquire patient-specific conductivity ratios to obtain accurate source localization.

Our results indicate that the source current distribution was affected by the shift of the conductivity ratio from 1/80 to 1/15, with the distribution less focused for the new 1/15 value. For higher noise levels, the center of mass error was also smaller for the 1/80 ratio. Thus, the previously accepted skull-to-brain conductivity ratio provided more focalized results and the reconstructed source current was less susceptible to high noise levels. The qualitative results with the clinical EEG data also showed a more focused SCD for the head model with the 1/80 skull-to-brain conductivity ratio. The more focused results may be explained by the increased resistivity of the skull tissue for the 1/80 ratio, causing the source current originating from the cortical pyramidal cells to spread further outwards as it crossed the skull, away from the original source location. An extended spread of current density in the volume conductor model would correspond to a more blurred potential distribution measured by the scalp electrodes in comparison to the Base Model. Therefore, for the inverse problem to account for the same potential distribution on the scalp calculated from the forward problem of the Base Model, the estimated SCD would be more focused for the 1/80 skull-to-brain conductivity ratio than for the 1/15 ratio. Based on the results obtained for CME and DF, the LORETA-like inverse method is more susceptible to noise if the new 1/15 skull-to-brain conductivity ratio is used. Quantitative and qualitative analysis imply that for low noise levels, the 1/15 ratio provides slightly improved localization, but still with lower spatial resolution.

The quantitative and qualitative results for the 1/15 and 1/30 skull-to-brain conductivity ratios were comparable, with a slight improvement in spatial resolution for

the 1/30 ratio. This indicates that slight patient-specific deviations in skull-to-brain conductivity ratios do not have a significant impact on source localization accuracy. Consequently, the new generally accepted value of 1/15 may be employed as the skull-to-brain conductivity ratio as long as the deviation within different patients does not vary to the extent of the previously accepted 1/80 value.

We performed a preliminary study on the effect of white matter anisotropy on source localization results. It has been shown that white matter anisotropy affects the forward problem for EEG analysis (Haueisen et al., 2002, Wolters et al., 2006). We extended this analysis by studying the effects of white matter orthotropic conductivity on inverse results. The quantitative and qualitative analyses suggest that the source current distribution was affected by orthotropic conductivity changes, which implies that white matter anisotropy will have an effect on the SCD of the inverse solution, specifically the magnitude of the current density.

## **6.2 *a priori* Constraints**

A common constraint in linear inverse methods is to set the orientation of the dipolar sources normal to the cortical surface (Dale and Sereno, 1993; Liu et al., 1998; Liu et al., 2002; Phillips et al., 2002a; Lin et al., 2006). This constraint is physiologically based on neural sources of measured scalp potential having an orientation perpendicular to the cortical sheet of the brain (Nunez, 1981). For the LORETA-like method used in this study, the normal orientation focused the source current distribution. Although the normal orientation constraint focused the solution energy, the center of the source activity was localized to the same site as with no orientation constraint. Based on these results,



the normal orientation constraint does not improve the localization accuracy, but it does improve the spatial resolution of the inverse method.

The more focused source current distribution may aid in defining a smaller area of the cortex for pre-surgical analysis for epileptic patients. Since the LORETA inverse problem method tends to produce blurred results, this reduction in the spatial extent of the foci is especially relevant. The study performed by Lin et al. (2006) did not directly measure the degree of focalization of the reconstructed SCD for the different inverse methods, but the qualitative results showed a more focalized SCD for most tests, which correspond with our findings. The localization error was also affected by the normal orientation constraint, which differs from our findings. However, different inverse methods were used in comparison to the LORETA method used in our study.

Another constraint that can improve the spatial resolution of source localization results is incorporating information from functional imaging techniques that measure blood flow. Because of its high spatial resolution, fMRI has the most promise for improving source localization results from EEG recordings (Liu et al., 1998; Dale et al., 2000; Gonzalez Andino et al., 2001; Jezzard et al., 2001; Wagner and Fuchs, 2001; Phillips et al., 2002a; Babiloni et al., 2003; Gotman et al., 2006; Liu et al., 2006). Since fMR images for epileptic patients are not always clinically available and are impractical for some ictal events, we studied the effect of constraining the inverse method with SPECT information, which is more clinically accessible and can currently measure both ictal and interictal events. Although SPECT can measure the blood flow changes caused by neural activity, it has a much lower spatial resolution than fMRI.

Because of the uncertainties between the origins of EEG and SPECT signals, SPECT information was used as a soft constraint for source localization (Liu et al., 1998; Dale et al., 2000; Gonzalez Andino et al., 2001; Wagner and Fuchs, 2001; Phillips et al., 2002a; Babiloni et al., 2003; Liu et al., 2006). We studied the effect of applying SPECT information with varying levels of weighting on the LORETA-like inverse problem: “strong”, “medium”, and “light” SPECT weighting. The different weights were tested for different scenarios: accurate *a priori* information with the SPECT constraint centered on the midpoint of the original source and inaccurate *a priori* information with the constraint placed away from the original source. The inaccurate *a priori* scenario corresponded to possible uncertainties that occur between the EEG and SPECT signals. Both of these scenarios were compared to source localization results without any SPECT constraint.

For the “strong” SPECT constraint, the reconstructed source current density was localized to within the region of the cortex with SPECT activation, and the EEG information was essentially disregarded. As the SPECT information moved away from the neural source location, the center of mass shifted with the increasing distance. Although the “strong” constraint led to a much lower center of mass error than no SPECT information for the accurate *a priori* scenario, especially as the noise levels increased, the center of mass error was much more substantial for the inaccurate *a priori* scenario. The distance between the SPECT information and the original source location had to be greater than 6cm with low noise levels before at least some activity was reconstructed in the correct location of the cortex. However, the majority of the reconstructed activity was still at the inaccurate SPECT location. The qualitative results agreed with these findings as well, with SCD reconstructed only within the region of the SPECT activity. For this

level of weighting, the source localization results were almost solely dependent on the SPECT information, and the inverse problem essentially disregarded the EEG potential distribution in reconstructing the source.

Based on these results, the “strong” weighting of 10 is not a viable option for functional image weighting such as SPECT. This agrees with Wagner and Fuch’s findings (2001), which showed that the LORETA inverse problem was unable to localize a source without a corresponding fMRI hotspot when the fMRI weighting was 10. However, Liu et al. (1998, 2006) have shown that the optimal weighting for fMRI in source localization was 90%, which is equivalent to the strong weighting performed in our analysis. This discrepancy may be due to analyzing the functional weighting with a different inverse method than from the LORETA approach used in this thesis.

Depending on how much emphasis of the SPECT information is desired, the functional weighting can be incorporated into the inverse problem either as a “medium” constraint of 2.5 or as a “light” constraint of 1.5. A “medium” weighting provided much more precise source localization results for the accurate *a priori* case, especially for higher noise levels. The compromise was that the center of mass might be further from the original source location for inaccurate SPECT information. Analysis of the validation metrics indicated that if the EEG noise level was low and the SPECT information was considered accurate, or if the noise level was high and the SPECT information was assumed to be within 4cm of the actual source location, the “medium” constraint provided improved source localization results. The qualitative results show that although the “medium” SPECT weighting did produce current density within the region of the cortex with neural sources, the magnitude of the SCD was particularly limited outside of

the SPECT area of activation. Thus, the “medium” constraint should be utilized only if the SPECT information is assumed reasonably accurate.

If confidence in the provided SPECT information is low, then the “light” weighting of 1.5 is recommended as a constraint on the inverse problem. Although this constraint provided minimal improvements in the center of mass error value for low noise levels, the source localization results were improved on to a larger extent with noisy EEG signals. As well, the center of mass did not shift significantly from the original source location for inaccurate SPECT information over all distances and all noise levels. The degree of focalization of the reconstructed source distribution also remained relatively high for small distances between the center of SPECT and dipolar activity. The qualitative results agree with these findings, with activity reconstructed in both the overlap region of SPECT and EEG activity as well as the region with only EEG activity. However, the spatial resolution of the source localization results may be limited by the spatial resolution of the SPECT information, as shown in the qualitative analysis.

The “light” constraint weighting of 1.5 provided moderate improvements in the source localization results without sacrificing accurate source localization for incorrect SPECT information. These results correspond with Wagner and Fuch’s findings (2001), which showed that for the LORETA problem, a weighting of 1.4 focalized the sources with corresponding fMRI hotspots while also reconstructing concentrated activity for the fMRI hotspot with no corresponding source. They also demonstrated that for weightings greater than 1.6, LORETA was incapable of reconstructing a source without the corresponding functional hotspot. Our results for a weighting of 1.5 indicate that although the source localization accuracy was influenced by SPECT activity outside the source

area, the LORETA inverse problem was still capable of reconstructing reasonably accurate source current density. Specifically, source activity without corresponding SPECT activity was still reconstructed with clinical EEG data. Thus, this “light” constraint provides a compromise between improving the source localization results with accurate functional information while maintaining reasonably accurate results for inaccurate functional information.

## Chapter 7

### Conclusions

We proposed analyzing the effects of both head model precision and *a priori* information on the accuracy of the EEG inverse problem. The motivation for this study was to determine the most accurate source localization results within the constraints of the present clinically available data from the University of Alberta hospital. Five different variations in the head model were analyzed in this study: electrode locations on the scalp, electrode distribution, CSF-skull tissue boundary placement, skull-to-brain conductivity ratio, and white matter orthotropic conductivity. The *a priori* information we investigated were including the normal orientation of the dipolar sources and incorporating functional information from SPECT imaging. In this work, the effect of both head model precision and *a priori* information was studied with the LORETA inverse problem.

Our results indicate that electrode placement errors do not have an effect on overall source localization accuracy, but may affect sources situated near electrodes with high position errors. The distribution of the electrodes has a major impact on the reconstructed source current distribution, especially if electrodes near the concentrated dipolar activity are excluded. Changing the location of the CSF-skull boundary and adjusting the skull-to-brain conductivity ratio by small amounts did not have a major influence on the localization accuracy. However, the source current density was affected by adjusting the skull-to-brain conductivity ratio from the previously accepted value of

1/80 to the new value of 1/15. Incorporating white matter orthotropic conductivity had a small influence on the reconstructed current density.

The *a priori* information had a strong effect on the source localization accuracy, with the normal orientation constraint focusing the reconstructed activity. The SPECT information provided more accurate source localization results as long it was used as a light constraint. However, spatial resolution of the reconstructed source current density was limited by the spatial resolution of the SPECT information. The SPECT constraint provided the biggest improvement in accuracy when the SPECT activity correlated with the source location.

In summary, we found in this study that:

- electrode placement errors do not affect overall source localization accuracy, but may affect sources near electrodes with high position errors;
- electrode distribution has a major impact on reconstructed source current distribution;
- segmentation error of the CSF-skull boundary do not have a major influence on localization accuracy;
- large variations in the skull-to-brain conductivity ratio affect the source current distribution;
- restricting sources normal to the cortical surface focuses the source current distribution; and
- utilizing SPECT information as a light constraint provides more accurate source localization results.

## **Future Considerations**

Expanding upon this study to incorporate current research areas that may improve source localization results and that may ultimately become available in a clinical setting would be ideal. This includes, but is not limited to, analyzing the effects of: fMRI information, skull (Ollikainen et al., 1999) and white matter anisotropy, and new MRI segmentation techniques. Further, the analysis of source localization accuracy could be expanded upon by calculating validation metrics for greater than one source activated at the same time. Since the LORETA method tends to produce blurred source current density, investigating a more accurate inverse method for analysis would be beneficial.



## Bibliography

- Awada KA, Jackson DR, Baumann SB, Williams JT, Wilton DR, Fink PW, Prasky BR. Effect of conductivity uncertainties and modeling errors on EEG source localization using a 2-D model. *IEEE Trans Biomed Eng* 1998;45:1135-1145.
- Babiloni F, Babiloni C, Carudcci F, Angelone L, Del Gratta C, Romani GL, Rossini PM, Cincotti F. Linear inverse estimation of cortical sources by using high resolution EEG and fMRI priors. *Int J Bioelectromag* 2001;3:1.
- Babiloni F, Babiloni C, Carducci F, Romani GL, Rossini PM, Angelone LM, Cincotti F. Multimodal integration of high-resolution EEG and functional magnetic resonance imaging data: a simulation study. *Neuroimage* 2003;19:1-15.
- Baillet S, Mosher JC, Leahy RM. Electromagnetic brain mapping. *IEEE Signal Proc Mag* 2001a;18:14-30.
- Baillet S, Riera JJ, Marin G, Mangin JF, Aubert J, Garnero L. Evaluation of inverse methods and head models for EEG source localization using a human skull phantom. *Phys Med Biol* 2001b;46:77-96.
- Baysal U, Haueisen J. Use of *a priori* information in estimating tissue resistivities – application to human data *in vivo*. *Physiol Meas* 2004;25:737-748.
- Benar CG, Gotman J. Non-uniform spatial sampling in EEG source analysis. Proc 23<sup>rd</sup> Conf IEEE-EMBS 2001;
- Berger H. Über das Electrenkephalogramm des Menschen. *Arch Psychiat Nervkrankh* 1929;87:527-570.
- Buchner H, Knoll G, Fuchs M, Rienäcker A, Beckmann R, Wagner M, Silny J, Pesch J. Inverse localization of electric dipole current sources in finite element models of the human head. *Electroenceph Clin Neurophysiol* 1997;102:267-268.
- Cuffin BN. Effects of local variations in skull and scalp thickness on EEG's and MEG's. *IEEE Trans Biomed Eng* 1993;40:42-48.
- Cuffin BN, Schomer DL, Ives JR, Blume H. Experimental tests of EEG source localization accuracy in realistically shaped head models. *Clin Neurophysiol* 2001;112:2288-2292.
- Dale AM, Sereno MI. Improved localization of cortical activity by combining EEG and MEG with MRI cortical surface reconstruction. *J Cognit Neurosci* 1993;5:162-176.

- Dale AM, Liu AK, Fischl BR, Buckner RL, Belliveau JW, Lewine JD, Halgren E. Dynamic statistical parametric mapping: combining fMRI and MEG for high-resolution imaging of cortical activity. *Neuron* 2000;26:55-67.
- Ding L, Lai Y, He B. Low resolution brain electromagnetic tomography in a realistic geometry head model: a simulation study. *Phys Med Biol* 2005;50:45-56.
- Duncan JS, Shorvon SD, Fish DR. *Clinical epilepsy*. New York: Churchill Livingstone, 1995.
- Ebersole J. Defining epileptogenic foci: past, present, and future. *J. Clin. Neurophysiol* 1997;14:470-483.
- Ferree TC, Eriksen KJ, Tucker DM. Regional head tissue conductivity estimation for improved EEG analysis. *IEEE Trans Biomed Eng* 2000; 47(12):1584-1592.
- Foster KR, Schwan HP. Dielectric permittivity and electrical conductivity of biological materials. In: Polk C, Postow E, editors. *CRC Handbook of biological effects of electromagnetic fields*. Boca Raton, FL: CRC Press, 1986:25-96.
- Fuschs M, Wagner M, Köhler T, Wischmann HA. Linear and nonlinear current density reconstructions. *J. Clin. Neurophysiol* 1999;16:267-295.
- Fuschs M, Wagner M, Kastner J. Boundary element method volume conductor models for source reconstruction. *Clin Neurophysiol* 2001;112:1400-1407.
- Geddes LA, Baker LE. The specific resistance of biological material – a compendium of data for the biomedical engineer and physiologist. *Med Biol Eng* 1967;5:271-293.
- Gencer NG, Acar CE. Sensitivity of EEG and MEG measurements to tissue conductivity. *Phys Med Biol* 2004; 49:701:717.
- Gonçalves S, de Munck JC, Verbunt JP, Bijma F, Heethaar RM, Lopes da Silva F. *In vivo* measurement of the brain and skull resistivities using an EIT-based method and realistic models for the head. *IEEE Trans Biomed Eng* 2003a;50:754-767.
- Gonçalves S, de Munck JC, Verbunt JPA, Heethaar RM, Lopes da Silva FH. *In vivo* measurement of the brain and skull resistivities using an EIT-based method and the combined analysis of SEF/SEP data. *IEEE Trans Biomed Eng* 2003b;50:1124-1128.
- Gonzalez Andino SL, Blanke O, Lantz G, Thut G, Grave de Peralta MR. The use of functional constraints for the neuroelectromagnetic inverse problem: alternatives and caveats. *Int J Bioelectromag* 2001;3:1.

- Gorodnisky IF, George JS, Rao BD. Neuromagnetic source imaging with FOCUSS: a recursive weighted minimum norm algorithm. *Electroencephalogr Clin Neurophysiol* 1995;95:231-251.
- Gotman J, Kobayashi E, Bagshaw AP, Benar CG, Dubeau F. Combining EEG and fMRI: a multimodal tool for epilepsy research. *J Magn Reson Imaging* 2006;23:906-920.
- Grave de Peralta-Menendez R, Gonzalez AS, Lutkenhoner B. Figures of merit to compare linear distributed inverse solutions. *Brain Topogr* 1996;9:117-124.
- Grova C, Daunizeau J, Lina JM, Bénar CG, Benali H, Gotman J. Evaluation of EEG localization methods using realistic simulations of interictal spikes. *NeuroImage* 2006;29:734-753.
- Hämäläinen M, Sarvas J. Realistic conductor geometry model of the human head for interpretation of neuromagnetic data. *IEEE Trans Biomed Eng* 1989;36:165-171.
- Hämäläinen M, Ilmoniemi R. Interpreting magnetic fields of the brain – minimum norm estimates. *Med Biol Eng Comput* 1994;32:35-42.
- Hansen PC, O’Leary DP. The use of the L-curve in the regularization of discrete ill-posed problems. *SIAM J Sci Comput* 1993;14:1487-1503.
- Haueisen J, Ramon C, Eiselt E, Brauer H, Nowak H. Influence of tissue resistivities on neuromagnetic fields and electric potentials studied with a finite element model of the head. *IEEE Trans Biomed Eng* 1997;44:727-735.
- Haueisen J, Tuch DS, Ramon C, Schimpf P, Wedeen VJ, George JS, Belliveau JW. The influence of brain tissue anisotropy on human EEG and MEG. *Neuroimage* 2002;15:159-166.
- Henry T, Duncan J, Berkovic S. *Advances in neurology: functional imaging in epilepsies*, v 83. Philadelphia: Lippincott, Williams & Wilkins, 2000.
- Hodgkin AL. *The conduction of the nervous impulse*. Springfield, Ill: CC Thomas, 1964.
- Huiskamp G, Vroeijsstijn M, van Dijk R, Wieneke G, van Huffelen A. The need for correct realistic geometry in the inverse EEG problem. *IEEE Trans Biomed Eng* 1999;46:1281-1287.
- Im CH, An KO, Jung HK, Kwon H, Lee YH. Assessment criteria for MEG/EEG cortical patch tests. *Physics in Med and Biol* 2003;48:2561-2573.
- Im CH, He B. On the accurate anatomical constraints in EEG/MEG source imaging. *Int J BioElec* 2006;8:1-11.

- Jasper HH. The ten-twenty electrode system of the International Federation. *Electroencephalogr Clin Neurophysiol* 1958;10:371-375.
- Jezzard P, Matthews PM, Smith SM. *Functional MRI: an introduction to methods*. Oxford: Oxford University Press, 2001.
- Kaiboriboon K, Lowe JL, Chantarujikapong SI, Hogan RE. The usefulness of subtraction ictal SPECT coregistered to MRI in single- and dual- headed SPECT cameras in partial epilepsy. *Epilepsia* 2002;43:408.
- Kavanagh RN, Darcey TM, Lehmann D, Fender DH. Evaluation of methods for three-dimensional localization of electrical sources in the human brain. *IEEE Trans Biomed Eng* 1978;25:421-429.
- Khosla D, Singh M, Don M. Spatio-temporal EEG source localization using simulated annealing. *IEEE Trans Biomed Eng* 1997;44:1075-1091.
- Khosla D, Don M, Kwong B. Spatial mislocalization of EEG electrodes – effects on accuracy of dipole estimation. *Clin Neurophysiol* 1999;110:261-271.
- Koles ZJ, Soong AC. EEG source localization: implementing the spatio-temporal decomposition approach. *Electroencephalogr Clin Neurophysiol* 1998;107:343-352.
- Lai Y, van Drongelen W, Ding L, Hecox KE, Towle VL, Frim DM, He B. Estimation of in vivo human brain-to-skull conductivity ratio from simultaneous extra- and intracranial electrical potential recordings. *Clin Neurophysiol* 2005; 116(2):456-465.
- Lantz G, Grave de Peralta R, Spinelli L, Seeck M, Michel CM. Epileptic source localization with high density EEG : how many electrodes are needed ? *Clin Neurophysiol* 2003;114:63-9.
- Lawson, CL, Hanson RJ. *Solving least squares problems*. Englewood Cliffs, NJ: Prentice-Hall, 1974.
- Lin F, Belliveau JW, Dale AM, Hämäläinen MS. Distributed current estimates using cortical orientation constraints. *Hum Brain Mapp* 2006;27:1-3.
- Liu AK, Belliveau JW, Dale AM. Spatiotemporal imaging of human brain activity using functional MRI constrained magnetoencephalography data: Monte Carlo simulations. *Neurobiology* 1998;95:8945-8950.
- Liu AK, Dale AM, Belliveau JW. Monte Carlo simulation studies of EEG and MEG localization accuracy. *Hum Brain Mapp* 2002;16:47-62.

- Liu Z, Kecman F, He B. Effects of fMRI-EEG mismatches in cortical current density estimation integrating fMRI and EEG: a simulation study. *Clin Neurophysiol* 2006;117:1610-1622.
- Logothetis NK, Pauls J, Augath M, Trinath T, Oeltermann A. Neurophysiological investigation of the basis of the fMRI signal. *Nature* 2001;412:150-157.
- Michel CM, Murray MM, Lantz G, Gonzalez S, Spinelli L, Grave de Peralta R. EEG source imaging. *Clin Neurophysiol* 2004;115: 2195-2222.
- Miller CE, Henriquez CS. Finite element analysis of bioelectric phenomena. *Crit Rev Biomed Eng* 1990;18:207-233.
- Mosher JC, Lewis PS, Leahy RM. Multiple dipole modeling and localization from spatio-temporal MEG data. *IEEE Trans Biomed Eng* 1992;39:541-557.
- Neilson LA, Kovalyov M, Koles ZJ. A computationally efficient method for accurately solving the EEG forward problem in a finely discretized head model. *Clin Neurophysiol* 2005;116:2302-2314.
- Nicholson, PW. Specific impedance of cerebral white matter. *Exp Neurol* 1965;13:386-401.
- Nunez PL. *Electric fields of the brain: the neurophysics of EEG*. New York: Oxford University, 1981.
- O'Brien TJ, O'Connor MK, Mullan BP, Brinkmann BH, Hanson D, Jack CR, So EL. Subtraction ictal SPECT co-registered to MRI in partial epilepsy: description and technical validation of the method with phantom and patient studies. *Nucl Med Commun* 1998;19:31-45.
- O'Brien TJ, So EL, Mullan BP, Hauser MF, Brinkmann BH, Jack CR, Cascino GD, Meyer FB, Sharbrough FW. Subtraction SPECT co-registered to MRI improves postictal SPECT localization of seizure foci. *Neurology* 1999;52:137-146.
- Ollikainen JO, Vauhkonen M, Kariäläinen PA, Kaipio JP. Effects of local skull inhomogeneities on EEG source estimation. *Med Eng Phys* 1999;21:143-54.
- Oostendorp TF, Delbeke J, Stegeman DF. The conductivity of the human skull: results of *in vivo* and *in vitro* measurements. *IEEE Trans Biomed Eng* 2000;47:1487-1492.
- Oostenveld R, Praamstra P. The five percent electrode system for high-resolution EEG and ERP measurements. *Clin Neurophys* 2001;112:713-719.

- Pascua J, Desco M, Rojo P, Santos A, Lopez J, Pozo MA. Spatial localisation of EEG dipoles in MRI using the 10-20 International System anatomical references. *IWISPA 2000*;151-156.
- Pascual-Marqui RD, Michel CM, Lehmann D. Low resolution tomography: a new method for localizing electrical activity in the brain. *Int J Psychophysiol* 1994;18:49-65.
- Pascual-Marqui RD. LORETA in 3D solution space. *ISBET Newsletter* 1995;6:22-28.
- Pascual-Marqui RD. Review of methods for solving the EEG inverse problem. *Int J Bioelectromagn* 1999;1:75-86.
- Phillips C, Rugg MD, Friston KJ. Anatomically informed basis functions for EEG source localization: combining functional and anatomical constraints. *Neuroimage* 2002a;16:678-695.
- Phillips C, Rugg MD, Friston KJ. Systematic regularization of linear inverse solutions of the EEG source localization problem. *Neuroimage* 2002b;17:287-301.
- Plonsey, R. Reciprocity applied to volume conductors and the ECG. *IEEE Trans Biomed Electron* 1963;10:9-12.
- Plonsey, R. *Bioelectric phenomena*. New York: McGraw-Hill, 1969.
- Rajagopalan S, Robb RA. Image smoothing with Savitzky-Golai filters. *Proc SPIE Int Soc Opt Eng* 2003;5029:773-781.
- Ramon C, Schimpf P, Haueisen J, Holmes M, Ishimaru A. Role of soft bone, CSF, and gray matter in EEG simulations. *Brain Topogr* 2004;16:245-248.
- Ramon C, Schimpf P, Haueisen J. Influence of head models on EEG simulations and inverse source localizations. *Biomed Eng Online* 2006; 5:10.
- Regan, D. *Human brain electrophysiology: evoked potentials and evoked magnetic fields in science and medicine*. New York: Elsevier Press, 1989.
- Rosenfeld M, Tanami R, Abboud S. Numerical solution of the potential due to sources in volume conductors with arbitrary geometry and conductivity. *IEEE Trans Biomed Eng* 1996;43:679-689.
- Rush S, Driscoll DA. EEG electrode sensitivity – an application of reciprocity. *IEEE Trans Biomed Eng* 1969;16:15-22.
- Scherg M, Von Cramon D. Evoked dipole source potentials of the human auditory cortex. *Electroencephalogr Clin Neurophysiol* 1986;65:344-360.

- Scherg M. Functional imaging and localization of electromagnetic brain activity. *Brain Topogr* 1992;5:103-111.
- Sharbrough F, Chatrian GE, Lesser RP, Luders H, Nuwer M, Picton TW. American electroencephalographic society guidelines for standard electrode position nomenclature. *J Clin Neurophysiol* 1991;8:200-202.
- Shorvon SD. *The treatment of epilepsy*, 2nd ed. Malden, Mass: Blackwell Science, 2004.
- Siegel AM. Presurgical evaluation and surgical treatment of medically refractory epilepsy. *Neurosurg Rev* 2004;27:1-18.
- Smith, SM. Fast robust automated brain extraction. *Human Brain Mapping* 2002;181:411-415.
- So, EL. Integration of EEG, MRI, and SPECT in localizing the seizure focus for epilepsy surgery. *Epilepsia* 2000;41(Suppl):S48-S54.
- Spencer, S. The relative contributions of MRI, SPECT, and PET imaging in epilepsy. *Epilepsia* 1994;35(Suppl):S72-S89.
- Towle VL, Bolanos J, Suarez D, Tan K, Grzeszczuk R, Levin DN, Cakmur R, Frank SA, Spire JP. The spatial location of EEG electrodes: locating the best-fitting sphere relative to cortical anatomy. *Electroenceph clin Neurophysiol* 1993;86:1-6.
- Tuch DS, Wedeen VJ, Dale AM, George JS, Belliveau JW. Conductivity tensor mapping of the human brain using diffusion tensor MRI. *Proc Natl Acad Sci USA* 2001; 98:11697-11701.
- Tyner FS. *Fundamentals of EEG technology*. New York: Raven, 1983.
- Uutela K, Hämäläinen M, Salmelin R. Global optimization in the localization of neuromagnetic sources. *IEEE Trans Biomed Eng* 1998;45:716-23.
- Wagner M, Fuchs M. Integration of functional MRI, structural MRI, EEG and MEG. *Int J Bioelectromag* 2001;3:1
- Wang MY, Maurer J, Calvin R, Fitzpatrick JM, Maciunas RJ. An automatic technique for finding and localizing external markers in CT and MR volume images of the head. *IEEE Trans Biomed Eng* 1996;43(3):627-637.
- Wang Y, Gottman J. The influence of electrode location errors on EEG dipole source localization with a realistic head model. *Clin Neurophysiol* 2001;112:1777-1780.

Withey, DJ. Dynamic edge tracing: recursive methods for medical image segmentation. Thesis. (PhD). University of Alberta 2006.

Wolters CH, Anwander A, Tricoche X, Weinstein D, Koch MA, MacLeod RS. Influence of tissue conductivity anisotropy on EEG/MEG field and return current computation in a realistic head model: a simulation and visualization study using high-resolution finite element modeling. *NeuroImage* 2006;30:813-826.

Zhang Y, Brady M, Smith S. Segmentation of brain MR images through a hidden Markov random field model and the expectation maximization algorithm. *IEEE Trans Biomed Eng* 2001;20(1):45-57.